Improved Internal Wave Spectral Continuum in a Regional Ocean Model

A. D. Nelson[1], B. K. Arbic[1], D. Menemenlis[2], W. R. Peltier[3], M. H. Alford[4], N. Grisouard[3], J. M. Klymak[5]

[1]Department of Earth and Environmental Sciences, University of Michigan, Ann Arbor, MI, USA
[2]Jet Propulsion Laboratory, California Institute of Technology, Pasadena, CA, USA
[3]Department of Physics, University of Toronto, Toronto, Canada
[4]Scripps Institution of Oceanography, University of California, La Jolla, CA, USA
[5]School of Earth and Ocean Sciences and Department of Physics and Astronomy, University of Victoria, Victoria, BC, Canada

Key Points:

- Internal gravity wave spectra in regional models are more realistic as model grid spacing decreases.
- The vertical wavenumber spectra improve less dramatically than the frequency spectra.
- Internal gravity wave consistency relations are applied to modeled spectra.

This is the author manuscript accepted for publication and has undergone full peer review but has not been through the copyediting, typesetting, pagination and proofreading process, which may lead to differences between this version and the Version of Record. Please cite this article as doi: 10.1029/2019JC015974

Corresponding author: Arin Nelson, dr.adnelson@gmail.com

Abstract

Recent work demonstrates that high-resolution global models forced simultaneously by atmospheric fields and the astronomical tidal potential contain a partial internal (gravity) wave (IW) spectral continuum. Regional simulations of the MITgcm forced at the horizontal boundaries by a global run that carries a partial IW continuum spectrum are performed at the same grid spacing as the global run and at finer grid spacings in an attempt to fill out more of the IW spectral continuum. Decreasing only the horizontal grid spacing from 2 km to 0.25 km greatly improves the frequency spectra and slightly improves the vertical wavenumber spectra of the horizontal velocity. Decreasing only the vertical grid spacing by a factor of 3 does not yield any significant improvements. Decreasing both horizontal and vertical grid spacings yields the greatest degree of improvement, filling the frequency spectrum out to 72 cpd. Our results suggest that improved IW spectra in regional models are possible if they are run at finer grid spacings and are forced at their lateral boundaries by remotely-generated IWs. Additionally, consistency relations demonstrate that improvements in the spectra are indeed due to the existence of IWs at higher frequencies and vertical wavenumbers when remote IW forcing is included and model grid spacings decrease. By being able to simulate an IW spectral continuum to 0.25 km scales, these simulations demonstrate that one may be able to track the energy pathways of IWs from generation to dissipation, and improve the understanding of processes such as IW-driven mixing.

Plain Language Summary

Models of internal waves (IWs) may help us to better understand the spatial geography of mixing in the ocean, and are playing an increasingly important role in the planning of satellite missions. Following recent work showing that high-resolution global models contain a partial IW spectrum, this paper describes further improvements in the spectrum seen in a high-resolution regional model forced at the boundaries by a previously-performed global IW simulation. Decreasing only the horizontal grid spacing greatly improves the frequency spectra and slightly improves the vertical wavenumber spectra of velocity. Increasing only the number of vertical levels does not yield any significant improvements. Decreasing both horizontal and vertical grid spacings yields the greatest improvement in both spectra. Our results suggest that regional models can exhibit improved internal wave spectra over global models if two conditions are met–they must have higher

horizontal and vertical resolutions, and they must have remotely generated IWs at their boundaries. Application of the so-called "consistency relations" demonstrates that the model is indeed carrying a field of high-frequency IWs. Being able to simulate a fuller IW spectrum demonstrates that one may be able to use these models to improve the understanding of IW-driven processes and energy pathways.

1 Introduction

Internal (gravity) waves (IWs) are a ubiquitious dynamical feature of any density-stratified fluid. First documented in the ocean by Nansen in his momentous Arctic expedition (Nansen, 1897), IWs have been at the forefront of both observational and theoretical ocean research continuously over the last century. Besides being a common feature in many in-situ and remote-sensing observations, they contribute to many important ocean processes such as mixing and acoustics. They also impact considerations for operational oceanography and remote-sensing satellite missions, particularly the upcoming Surface Water and Ocean Topography (SWOT) wide-swath altimeter mission (Fu et al., 2012).

As IWs in the linear regime obey well-known dispersion laws, they are often studied in Fourier space; i.e. in terms of frequency and wavenumber rather than time and space. Garrett and Munk (1972, 1975) produced an empirical model of the full frequency-wavenumber spectrum of oceanic IWs assuming a homogeneous and statistically stationary ocean. This model of the IW spectral continuum, referred to here as the GM76 spectral model, is still in wide use today, although several improvements have been subsequently suggested (e.g., Garrett and Munk, 1979; Levine, 2002).

Demonstrating that the GM76 spectrum appears naturally as a ubiquitous feature of numerical ocean models has remained a primary goal of theoretical research. However, the spectrum strongly depends on the actions of nonlinear and small-scale dynamics to move energy from the large-scale forcings, e.g., surface winds and tides, to the smaller scales in which the continuum of spectral energy resides. This inherent complexity presents an obstacle for simulating a full IW spectrum in global- and basin-scale models.

Global modeling of the IW continuum spectrum is still in its infancy, and the available models have their own advantages and disadvantages. A summary of recent state-of-the-art global IW continuum modeling efforts, which build upon efforts to include the

astronomical tidal potential in high-resolution ocean general circulation models (e.g., Arbic et al., 2010; Rocha et al., 2016) is provided in Arbic et al. (2018). The first demonstration that a partial IW continuum spectrum exists in global models was by Müller et al. (2015), who compared frequency spectra in models to moored observations, and found that the frequency-horizontal wavenumber spectra of the model's horizontal kinetic energy follows expected IW dispersion curves. The HYbrid Coordinate Ocean Model (HYCOM; Chassignet et al., 2009) simulations discussed in Müller et al. (2015) have been vetted against many observations, and have internal tide energy levels that match those in altimetry reasonably well (e.g., Shriver et al., 2012). The MIT General Circulation Model (MITgcm; Marshall et al., 1997) simulation employed as the basis for this study, denoted as LLC4320 (Rocha et al., 2016), has weaker near-inertial kinetic energy and stronger internal tidal kinetic energy at the ocean surface when compared to drifter observations (Yu et al., 2019). However, the IW spectral continuum of the LLC4320 simulation lies closer to observations than does the continuum in the global HYCOM simulations (Savage et al., 2017).

Due to the potential importance of IW models for gaining a better understanding of ocean mixing, acoustics, and satellite measurements, it is natural to examine the further improvements to the IW continuum spectra seen in higher-resolution models. Because decreasing the grid spacing of the models increases the computational workload required to integrate the models, modelers often simulate regional domains rather than the entire globe. One such effort (Mazloff et al., 2020) attempted this feat and found that their IW spectra are significantly lacking, especially at higher frequencies. It is suspected that this is due to missing IWs that are generated outside the domain that propagate to the region of interest, contributing to the IW spectrum inside the region. Therefore, it is natural to attempt to further improve the IW continuum spectra seen in regional models by forcing them at their boundaries by the global internal wave models. This manuscript documents improvements in the IW spectrum of a regional model run with lateral boundary conditions taken from a global IW model, and with horizontal and vertical grid spacings that are finer than can be achieved in today's state-of-the-art global models.

There are many practical applications for models that can better simulate the IW spectral continuum beyond aiding research in large-scale topics such as acoustics and satellite measurements. For example, the simulation of an IW spectral cascade down to finer spatial scales may allow one to track the energy pathways of IWs from generation to dis-

sipation along the lines of fine-scale parameterizations applied to observations (Polzin et al., 1995). Ultimately, one may be able to use IW models to study the spatial geography of IW-driven mixing, which in turn impacts the large-scale oceanic circulation (e.g., Munk & Wunsch, 1998).

2 Observations and Numerical Simulations

This study utilizes observations and MITgcm simulations of a region northwest of Hawaii bounded by 24°-32°N, 193°-199°E, characterized by an IW beam that is generated by tidal forcing over a region of shallow (<1000m) topography, the French Frigate Shoals, in its southwest corner. This domain was partially instrumented in Spring 2006 in the context of the Internal Waves Across the Pacific (IWAP) experiment (Alford et al., 2007). A collection of observations from six McLane Moored Profilers (MMPs; Morrison III et al., 2001) from IWAP are available; four are within the defined domain. The MMP observations are described in more detail in Section 2.1. The MITgcm simulations performed within this domain are described in Section 2.2.

2.1 MMP Observations

The MMPs measure pressure, temperature, salinity, and three-dimensional velocity via a sensor array that travels up and down a moored wire. For the MMP observations analyzed here, measurements are taken between approximately 90m and 1500m over a period of about 50 days (depending on the instrument in question) with a sampling interval of approximately 1.5 hours. The locations of the profilers within the analysis domain are displayed in Figure 1, numbered in order from southern-most to northern-most. The MMP data are calibrated, processed, and linearly interpolated onto standardized depth levels set 2 dbar apart (Toole, 2001). The high vertical resolution of the MMP data make them ideal for examining vertical wavenumber spectra. These data have been analyzed in numerous publications (Alford et al., 2007; Zhao et al., 2010; MacKinnon et al., 2013; Alford et al., 2017; Luecke et al., 2017; Savage et al., 2017).

Periods in the MMP observations containing gaps longer than 6 hours are discarded. The MMP observations are slightly asynchronous in time, so they are linearly interpolated onto even time steps 1.5 hours apart. Any obvious outliers in visual inspections

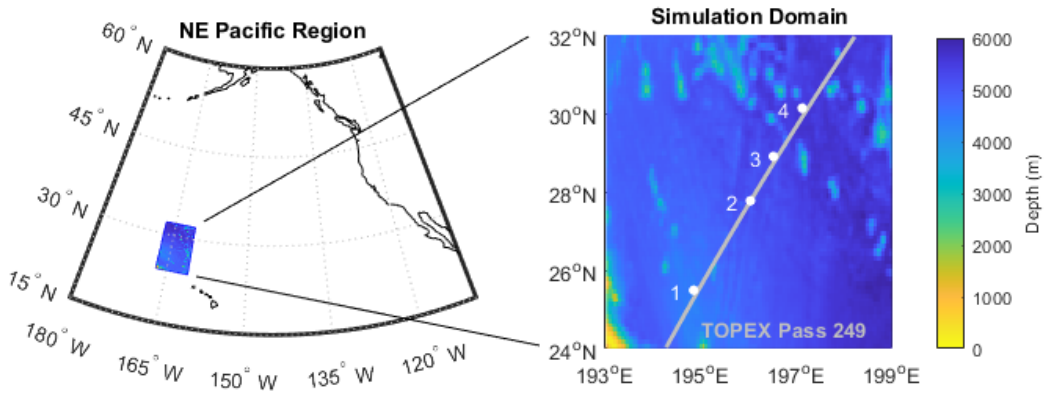

Figure 1. (Left) The Northeast Pacific region showing a colored box at the location of the simulation domain. (Right) A close-up of the simulation domain including the local bathymetry (color), the locations of the MMPs (white dots), and the trajectory of TOPEX-Poseidon satellite pass #249 (gray line).

are removed, and any remaining gaps in the data are filled in via linear interpolation. The details of these processed observational records are listed in Table 1.

Profiler (#)	Location (°N, °E)	z Range (m)	z Span (m)	t Range (d.o.y.)	t Span (days)
1	25, 195	88–1398	1310	115–151	36
2	28, 196	94–1396	1302	141–150	9
3	29, 197	88–1402	1314	139–165	26
4	30, 197	94–1400	1306	115–137	22

Table 1. Locations in latitude and latitude (°N, °E), depths (z), and times (t) of uninterrupted MMP data availability. d.o.y. denotes day-of-year (for a non-leap year). All values are rounded to the nearest integer.

Vertical velocity in the ocean is generally much smaller than platform motion and hence immeasurable except from bottom-mounted platforms. The MMP is no exception; hence, vertical velocities from the observations are not considered in this work.

2.2 Model Output

The global circulation model output employed as the basis for this study is the MITgcm simulation denoted by MITgcm48 in some previous publications (e.g., Savage et al., 2017) and LLC4320 in others (e.g., Rocha et al., 2016; Qiu et al., 2018). Here, it will be referred to as LLC4320. This simulation was run in the hydrostatic configuration with a nominal 1/48° horizontal grid (2.3km near the equator, 0.75km at high latitudes) and 90 depth levels from the free surface to seafloor depths up to 7000m with thicknesses increasing from 1.0m at the surface level to 480m at the bottom level. The ocean surface is forced with the six-hourly atmospheric fields from the 0.14° European Center for Medium-Range Weather Forecasts (ECMWF) atmospheric operational model analysis. Starting on the first day of 2011, ECMWF output is converted to surface fluxes (Large & Yeager, 2004), providing forcings from atmospheric wind, pressure, and buoyancy. This continues for the yearly duration of the model run. Note that the wind power from these fields may be under-represented in the simulations, as discussed by (Yu et al., 2019) and references therein. A sea ice model (Losch et al., 2010) is used to compute ocean surface fluxes over ice-covered regions. Astronomical tidal forcing, provided by the full lunisolar potential, is applied to MITgcm as an additional atmospheric pressure forcing (Ponte et al., 2015).

The new regional simulations performed for this study are driven by the same atmospheric fields at the ocean surface. A hard boundary condition is applied at the lateral boundaries, in which the model variables (e.g., temperature, salinity, and velocities) at every depth level are set to be directly equal to the LLC4320 hourly output. While simple to implement, a hard boundary condition may cause kinetic energy buildup and wave reflections at and near the boundaries. The hourly time stepping of the boundary conditions from the global model may also create a pulsing signal with a frequency of 24 cpd and its harmonics that will propagate throughout the simulation domain. Visual comparisons of animations from LLC4320 and the regional simulations are performed to ensure that the boundary condition choices do not produce any strong reflections or other anomalous features. All regional simulations are performed on the Niagara supercomputing cluster operated by SciNet at the University of Toronto (Ponce et al., 2019).

The first simulation (denoted "One-To-One") is performed at the same horizontal and vertical grid spacings as the global LLC4320 simulation to determine if the bound-

	LLC4320	One-To-One	Finer-Δz	Finer-Δx	Finer-Both
Δx (km)	2	2	2	1/4	1/4
# Levels	90	90	270	90	270

Table 2. The nominal horizontal grid spacing (Δx) and number of vertical depth levels of the MITgcm simulations utilized in this work. LLC4320 is a global simulation, and is used to force the boundaries of the other regional simulations.

ary effects significantly impact the regional simulation. Simulations are then run with finer grid spacings, including one at a finer vertical grid spacing of 270 levels (denoted "Finer-Δz"), one at a finer horizontal grid spacing of 250m (denoted "Finer-Δx"), and one where both horizontal and vertical grid spacings are made finer by these amounts (denoted "Finer-Both"). The spatial configurations of these simulations are summarized in Table 2.

For all but the Finer-Both simulation, a time step size (Δt) of 25 seconds is used, the same as that used in LLC4320. In the Finer-Both simulation, small-scale processes cause the simulation to become unstable at this Δt at some point during the integration. When this instability is flagged by the model, the simulation is stopped, Δt is decreased, and the simulation is resumed from the beginning of the day in which the instability occurred. This stopping and restarting of the model integration occurs multiple times, resulting in a median Δt of 10 seconds and a minimum Δt of 6 seconds. These Δt's are important to keep in mind when exploring internal waves; the wavelengths and frequencies of the internal waves that can be simulated by the model are limited by the spatial grid spacing and size of the integration time step. Note that in every case the "sampling" frequency of the model output (one output every 10 minutes, or 144 outputs per day) is a multiple of the model's integration frequency. Additionally, this finer output interval (versus hourly from LLC4320) allows for higher frequencies to be studied; a point that will become important later in the analyses.

3 Methods

3.1 Data Processing

The depth levels in the global MITgcm simulations were historically chosen to obtain the best representation of the mixed-layer and thermocline, and IWs were not a primary concern. The increasing thickness of the vertical levels at greater depths may produce aliasing, damping, or reflecting of high vertical wavenumber motions as they propagate downwards into deeper regions with layer thicknesses longer than the associated wavelengths. To mimic the effects of the coarse vertical discretization in the model, the observations are processed in three separate ways; at the full observational resolution of 2 dbar, averaged within the global model depth levels (90 levels), and averaged within the finer-grid regional model depth levels (270 levels). The model-level-averaged observations were computed by averaging all the observations at depths between the upper and lower bounds of each depth level. These processed observations are referred to as Obs.-Coarse and Obs.-Fine respectively.

From the model outputs, time series of temperature, salinity, and three-dimensional velocity are taken at the MMP locations and truncated to the time span of the corresponding observations taken at that location. It should be noted that these time spans, while being equal in length, are not contemporaneous with the observational records. In the vertical, the model outputs are truncated to the depth levels that are fully contained within the vertical limits of the corresponding observational record. In both the observations and truncated model outputs, temperature and salinity are used to compute potential density and buoyancy frequency using the Thermodynamic Equation of Seawater 2010 (McDougall & Barker, 2011).

To account for changes in stratification in depth and time, the data may be Wentzel-Kramers-Brillouin–Jeffreys (WKBJ) scaled (Leaman & Sanford, 1975). This scaling transforms the data into a coordinate system in which the mean and variability of the stratification, and consequently the buoyancy frequency N, is constant in depth. WKBJ scaling is based upon the use of the dimensionless factor $n(z) = \sqrt{\overline{N^2(z)}/N_0^2}$, in which $\overline{N^2(z)}$ denotes the all-time mean of $N^2(z,t)$ at depth z and N_0 is a constant reference value. While the choice of N_0 is arbitrary, a value of 72 cpd is used for convenience. Other possible choices of N_0 do not drastically affect the results (Alford & Whitmont, 2007), and a constant value for all four locations is employed.

Given this definition of $n(z)$, the zonal, meridional, and vertical velocities (U, V, and W respectively) are scaled by dividing the horizontal velocities by $\sqrt{n(z)}$, and by multiplying the vertical velocities by this same factor. The depths are also WKBJ-stretched using $z' = \int n(z)\, dz$ with the upper limit set to 100m at all locations. For the rest of this paper, all variables and results are assumed to be WKBJ-scaled unless otherwise noted. Also, note that extra care should be taken in interpreting these spectra as they are no longer in Cartesian coordinates.

3.2 Spectral Calculations

Power spectral densities (shortened to "spectra" in this work) are computed using the classical Fourier transform method in time and using the Lomb-Scargle periodogram method (Lomb, 1976; Scargle, 1982) in depth; the latter accounts for uneven vertical sampling and/or uneven WKBJ stretching. The Nyquist wavelength was chosen to be twice the smallest vertical spacing of the associated data. This procedure is performed for both the complex horizontal rotary velocity $\mathcal{Z}(z,t) = U(z,t) + iV(z,t)$ and the vertical velocity W. The form of the Lomb-Scargle periodogram for complex series is derived in Bretthorst (2003), which simplifies to a linear-least-squares fit of sinusoids since U and V are sampled simultaneously. Spectra are computed over 6.85-day windows with 50% overlap; a non-integer-day window length was chosen to limit the possibility of aliasing of near-inertial and tidal signals with frequencies of an integer or near-integer multiple of 1 cpd. No windowing is done in depth due to the limited number of vertical levels in the simulations that span the depth range of the observations; about 30 and 90 for the 90-level and 270-level configurations respectively.

According to linear wave theory, the spectra of rotary velocity are expected to be red in both frequency and vertical wavenumber. Since Fourier transforms expect the data to be a sum of sinusoids, this redness can introduce a bias when these sinusoids are fit to the data. This bias, also known as spectral leakage, is accounted for here by applying pre-whitening to the spectral computations of $\mathcal{Z}$ by multiplying each Fourier coefficient by the factor $\omega m \mathrm{sinc}(\omega dt)\mathrm{sinc}(mdz)$, where the frequency ω and vertical wavenumber m are in units of cycles per unit time and unit depth respectively, dt is the time step size, and dz is the smallest vertical spacing. The pre-whitening is done individually for each time window. The resulting spectra are averaged together and then recolored by dividing the averaged spectra by the factor $|(2-2\cos(\pi\omega dt))(2-2\cos(\pi m dz))|$. These

spectra, which have units of squared velocity per unit frequency and vertical wavenumber, are henceforth referred to as kinetic energy spectra. Upper and lower 95% confidence bounds are computed using traditional means and subjected to the same pre-whitening procedure.

3.3 Consistency Relations

As first detailed in Fofonoff (1969), for an arbitrary field of freely-propagating linear waves, there exists a complete set of linearly independent spectral and cross-spectral relations called consistency relations. In statistical tests, the consistency relations are used to quantify the confidence that the variability in a set of data can be explained by a wave field with the corresponding relations. A summary of the consistency relations for an oceanic IW field is detailed in Table 1 of Müller and Siedler (1976) as well as in Table 3 of Lien and Müller (1992). An application of these consistency relations to observational data is recorded in Müller et al. (1978). Since these relations are derived from linear IW theory, they are independent of any spectral model choice, GM76 or otherwise.

While there are many consistency relations that can be tested, for the sake of simplicity, only two are used in this work. These are the ratio of the counter-clockwise (CCW) to clockwise (CW) horizontal kinetic energy spectra, and the ratio of the vertical to horizontal kinetic energy spectra:

$$\frac{S^+}{S^-} = \left(\frac{\omega - f}{\omega + f}\right)^2 \tag{1}$$

$$\frac{N^2}{\omega^2}\frac{S^0}{S^- + S^+} = \frac{\omega^2 - f^2}{\omega^2 + f^2} \tag{2}$$

where f and N are the local inertial and buoyancy frequencies, S^+/S^- is the frequency (ω) spectra of $\mathcal{Z}$ at positive/negative values of ω, corresponding to CCW/CW rotation in time, and S^0 is the frequency spectrum of vertical velocity. Equation 2 is written in such a way that the value of the consistency relation approaches unity for $f \ll \omega \ll N$. These consistency relations are written for a hydrostatic ocean; for a non-hydrostatic ocean, Equation 2 has an additional multiplicative factor of $N^2/(N^2-\omega^2)$ on the right-hand side.

In this work, to avoid complications of a varying stratification with depth, the frequency spectra used to evaluate these consistency relations are computed individually at each depth using the non-WBKJ-scaled time series (a windowing of 6.85 days with

50% overlap is still employed). $\overline{N^2(z)}$ at the respective depth is used in computing the theoretical value of the consistency relation in Equation 2.

3.4 A Note on the Dispersion Relation versus Model Grid Spacing

The simulated IW spectrum is strongly dependent on the model grid spacing. For a given Δx, decreasing Δz in turn increases the upper limit of the ω that can be simulated. For example, for a vertical wavelength of 100m, the model configuration with $\Delta x =$ 2000m can only simulate IWs up to a limit of $\omega \approx 36$ cpd according to the dispersion relation assuming a buoyancy frequency equal to $N_0 = 72$ cpd. When $\Delta x = 250$m, this limit increases to $\omega \approx 134$ cpd, which is greater than the time-mean value of N at nearly all depths in the observations and simulations within the domain used in this work.

Another way to explore this issue of relating Δx and Δz is in the context of orthogonal vertical modes. For any given vertical mode, there is a prescribed horizontal and vertical wavelength associated with that mode. At high modal numbers, if the grid spacing in one dimension is not sufficient to resolve a given mode, it is unclear how the dynamics associated with that mode in the other dimension are affected. This concept was recently explored in the context of atmospheric modeling (Stewart et al., 2017), which found that there should be at least 2π vertical layers between the zero crossings of a given vertical mode in order for that mode to be accurately simulated. Stewart et al. (2017) then used this concept to prescribe the number of vertical layers in their model given its horizontal resolution using the relationship between the horizontal and vertical wavelength of a given vertical mode as previously mentioned. This concept was not initially considered when choosing the model grid spacings used in this work, but, as will be seen, such constraints on model grid spacing may need to be more carefully followed in future high-resolution oceanic IW simulations.

4 Results & Discussions

4.1 First Look

To get an idea of the dynamical properties at the southern-most MMP location, and to get an early insight into the model-data agreement, record-length means of temperature, salinity, buoyancy frequency, and velocity are shown in Figure 2. These data

are not WKBJ-scaled. These results, along with the results in the following subsections, are similar at the other MMP locations. Thus, for the sake of brevity, we will only show results at the southern-most MMP location in this paper.

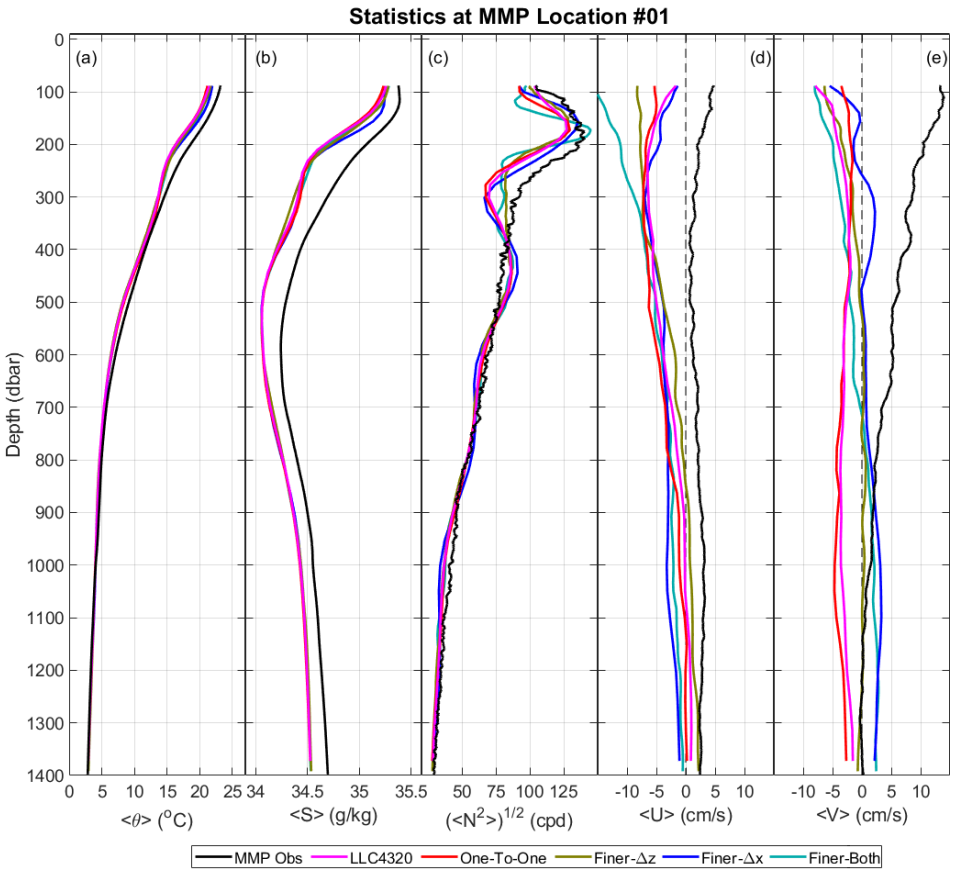

Figure 2. The time mean over the observational period of the variables of interest at the southern-most MMP location from all data sources. These variables include (a) temperature, (b) salinity, (c) buoyancy frequency (computed as the root-mean-square), (d) zonal velocity, and (e) meridional velocity. These results are not WKBJ-scaled.

Figure 2 indicates that the thermodynamic variables display reasonable agreement between the observations and simulations, which both exhibit the strongest vertical gradients of temperature and salinity between 100m and 300m depth. The observed and simulated mean velocities are opposite in sign, with the simulations exhibiting a stronger mean velocity in the zonal direction and a weaker mean velocity in the meridional direction relative to the observations. However, as will be shown, the standard deviation of the velocities are larger than their means at nearly all depths, so this result is not sta-

tistically significant. Additionally, the record length is short relative to the timescales of intrinsic variability in this region due to structures such as mesoscale eddies. Since the model is not data-assimilative, there is no reason to expect these larger, slower structures to match between the model and the real world over this short time period, so this sign reversal in the mean flow is not surprising.

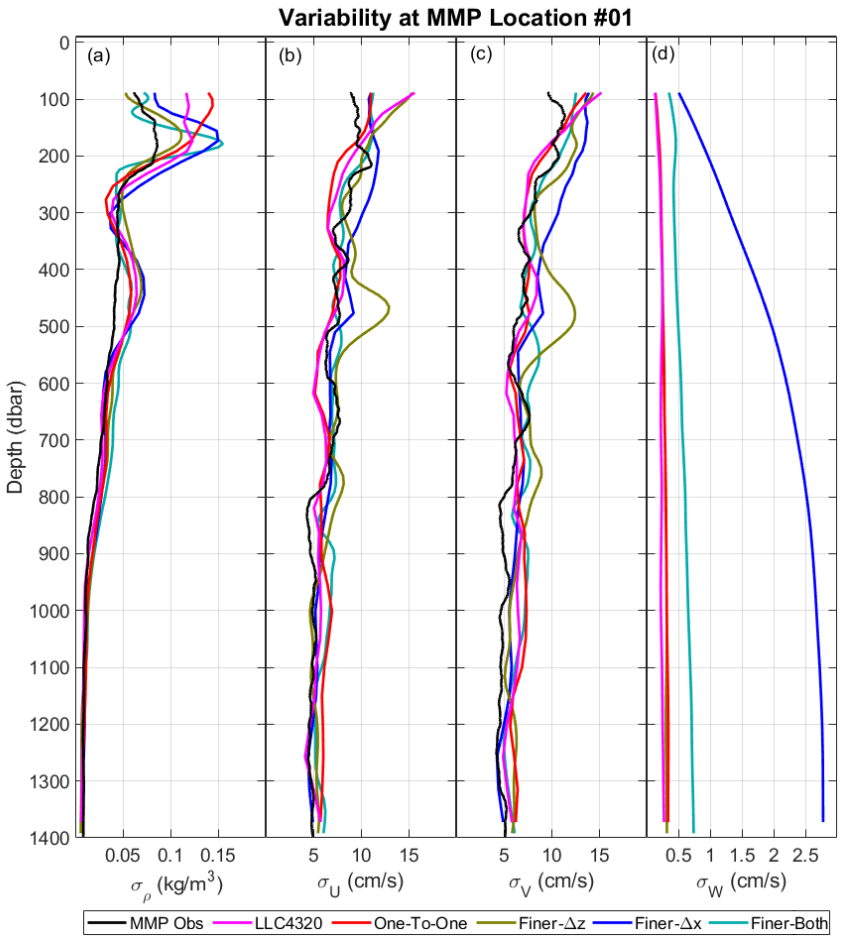

Figure 3. The temporal standard deviations of the (a) potential density, (b) zonal velocity, (c) meridional velocity, and (d) vertical velocity at the southern-most MMP location from all data sources. Velocities are not WKBJ-scaled.

The temporal standard deviations of the non-WKBJ-scaled potential density and velocities are shown in Figure 3. As explained previously, vertical velocities from the MMPs are disregarded in this study. Below 300m, the variabilities of the velocities are fairly con-

stant in depth with magnitudes that are comparable between the observations and all simulations, with the simulations showing a slightly stronger variance overall. In contrast, the variability in the vertical velocity varies significantly depending on the model grid spacings. For the Finer-Both simulation, the variability in the vertical velocity is about twice as large as the vertical velocity variability in the LLC4320, One-To-One, and Finer-Δz simulations at all depths. The vertical velocity in the Finer-Δx simulations is significantly more variable relative to the other simulations. This striking increase in the vertical velocity when only the horizontal grid spacing is decreased may or not be be due to a mismatch between the horizontal and vertical model grid spacings as discussed in Section 3.4.

4.2 Frequency - Vertical Wavenumber Rotary Spectra

Figure 4 displays the frequency-vertical wavenumber spectra of the observations, LLC4320, and the four MITgcm runs performed on the Niagara supercomputer. All simulations show a large amount of variance at the near-inertial, diurnal, and semidiurnal frequencies. The peaks at these frequencies are indicative of forcing from the winds and the astronomical tidal potential. There is a strong asymmetry between clockwise (CW) and counterclockwise (CCW) rotating velocities, with both the observations and simulations showing more energy at the CW forcing frequencies rather than CCW. This asymmetry is as expected in the Northern Hemisphere, and it is important that, before anything else, one verifies that the simulations capture this CW/CCW asymmetry.

In the One-To-One simulation, the spectrum has a majority of the variance residing within peaks near the forcing frequencies and their harmonics, compared to the observations which have variance spread out across the spectral continuum. This "peakiness" may be indicative of a lack of nonlinear interactions in this simulation necessary to transfer energy from these low-frequency bulk motions into the high-frequency IWs.

When the vertical grid spacing is decreased, the spectra remain similar to that of the One-To-One simulation, although more variance is present at higher vertical wavenumbers. When the horizontal grid spacing is decreased, there is a similar effect, except that more variance is present at higher frequencies and in between the forcing bands and harmonics, while the spectrum still exhibits the "peakiness" of the One-To-One spectrum. When both horizontal and vertical grid spacings are decreased, the spectrum becomes

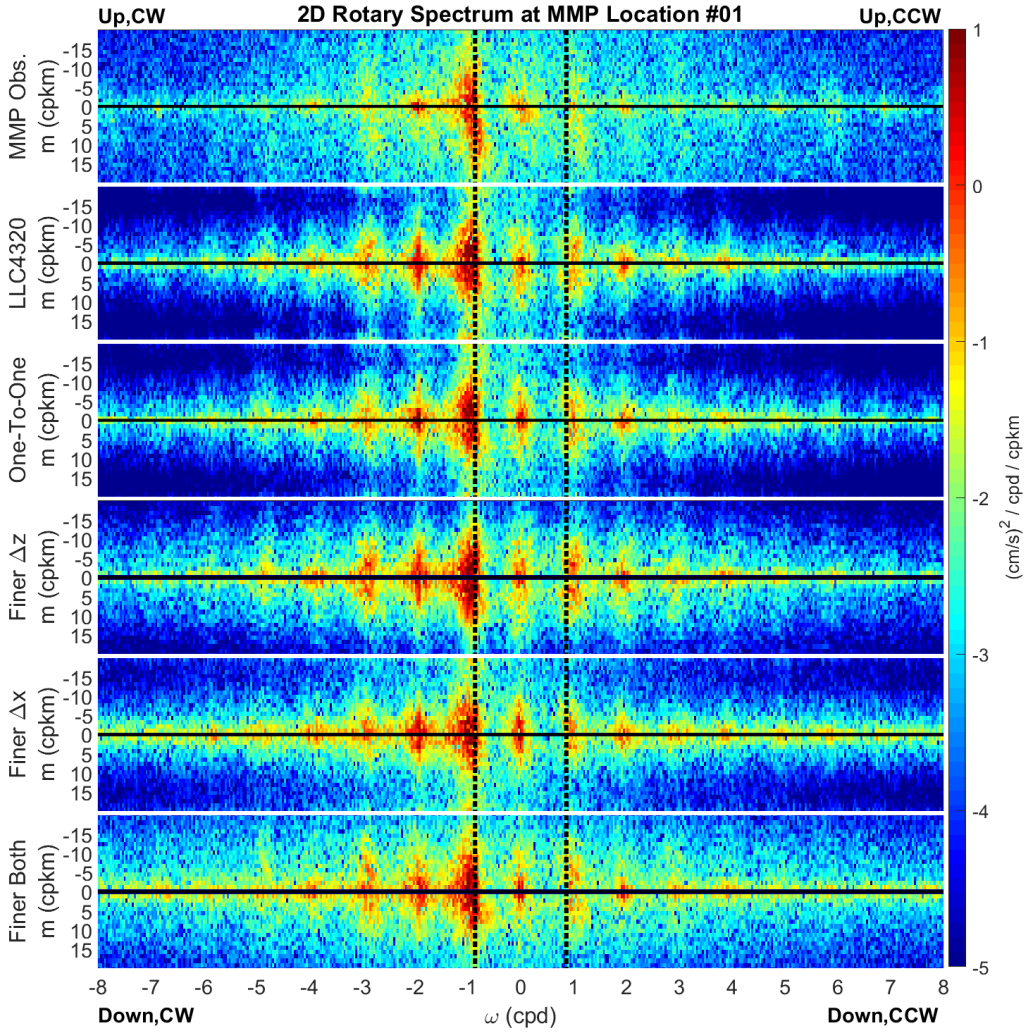

Figure 4. The 2D WBKJ-scaled frequency-vertical wavenumber spectrum of horizontal kinetic energy at the southern-most MMP location for the observations (top 1) and the MITgcm simulations (bottom 5). Dashed lines indicate the local inertial frequency. Positive/negative frequencies indicate CCW/CW rotation in time. Positive/negative vertical wavenumbers indicate CCW/CW rotation in (WBKJ-stretched) depth. The peaks are typically present at inertial and tidal frequencies and their higher-order harmonics.

much more comparable to that seen in the observations, with much less "peakiness" at the forcing frequencies and much more energy spread out into the continuum, especially at higher vertical wavenumbers.

One troubling feature is the noticeable increase in variance with vertical wavenumber at high vertical wavenumbers. This increasing variance at high vertical wavenumbers only occurs at wavelengths shorter than the coarsest vertical spacing, so this increase in variance is attributed to either aliasing from lower wavenumbers or from model "speckling", an instability where grid points have alternating positive and negative values that flip sign and increase in amplitude with each time step. We do not know whether this is due to failure of the hydrostatic assumption or some other aspect of the model.

4.3 Frequency Power Spectra

The total (CW plus CCW) horizontal kinetic energy frequency spectra at 620m are shown in Figure 5. The separate frequency spectra of CCW and CW horizontal kinetic energy and vertical kinetic energy are shown in Figure 6. In Figure 7, the theoretical and measured consistency relations in Equations 1 and 2 are displayed. The 90% confidence interval (5% to 95% confidence limits) of the consistency relations are computed using a million-member bootstrap based on the confidence intervals of the associated spectra and are denoted by the shaded regions. WBKJ scaling assumes $\omega \ll N$, but this isn't always true for the simulation output which has an integration frequency exceeding the time mean of N at some depths. Thus, only the frequency spectra of the non-WBKJ-scaled data are explored here. The spectra are also smoothed in log-log space to aid in visually separating the curves.

From Figure 5 and Figure 6 (a) and (b), it is apparent that the variance of horizontal velocity, and its partitions into CW and CCW components, is similar between the observations and all of the simulations up to frequencies at about 5 cpd. The observations are different in that there is less variance at the forcing peaks and more variance in the continuum. This "peakiness" is consistent with a lack of nonlinear small-scale dynamics in the simulations as previously discussed.

At frequencies higher than about 5 cpd, the spectra of the simulations with the coarser horizontal grid spacing begin to decrease relative to the observations, the finer horizontal grid spacing simulations, and the GM76 model. There are some noticeable peaks near

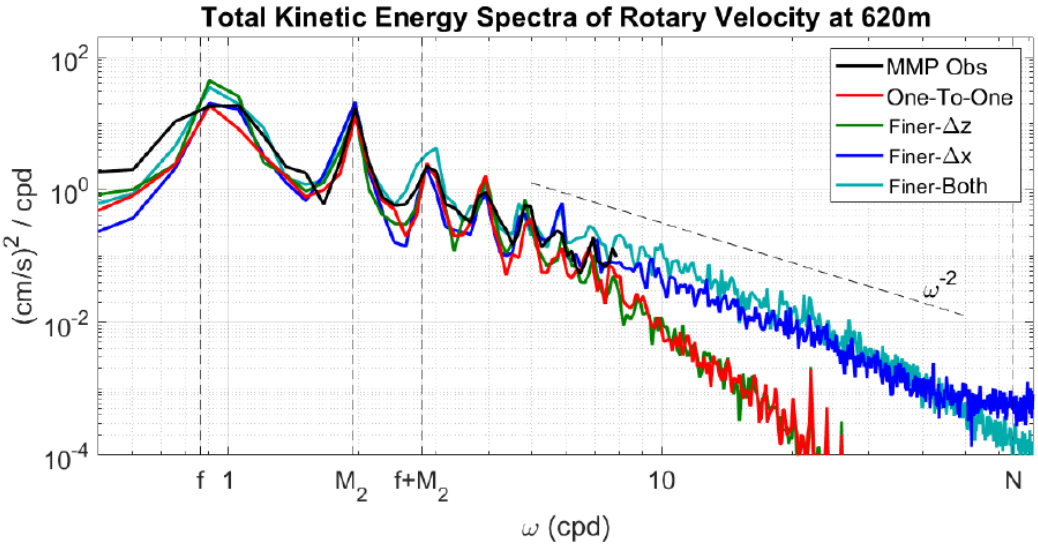

Figure 5. The total (CW plus CCW) horizontal frequency spectra at 620m depth at the southern-most MMP location. These spectra are not WKBJ-scaled. There are marks on the x-axis for the inertial frequency f, the semidiurnal lunar tide M_2, their sum $f + M_2$, and the buoyancy frequency from the observations N (computed as the root of the time mean of N^2). The dashed curve above the spectra represents the spectral slope theorized by the GM76 model.

24 and 48 cpd, likely due to the hourly forcing at the simulation boundaries, and near the Nyquist frequency of 72 cpd due to model speckling, but even with these peaks the spectra still do not rise to the variance of the Finer-Δx and Finer-Both spectra, and are hence not visible in Figure 5 and Figure 6 (a) and (b). Comparatively, the Finer-Δx simulation retains a GM76 model-like spectral slope of approximately ω^{-2} out to about 50 cpd, after which it begin to flatten. The Finer-Both simulation maintains a slope of ω^{-2} out to the "Nyquist" frequency associated with the model output frequency; 72 cpd.

In the vertical kinetic energy spectra of Figure 6 (c), once again the spectra from the simulations with coarser horizontal grid spacings begin to decrease relative to the simulations with finer horizontal grid spacing after about 5 cpd. However, the Finer-Δx simulation exhibits a higher vertical velocity variance and a spectral slope shallower than ω^{-2} at all frequencies. It is unknown whether the differences in the Finer-Δx simulation's vertical velocity spectrum relative to the other simulations is the result of a possible artifact as described previously or some other mechanism.

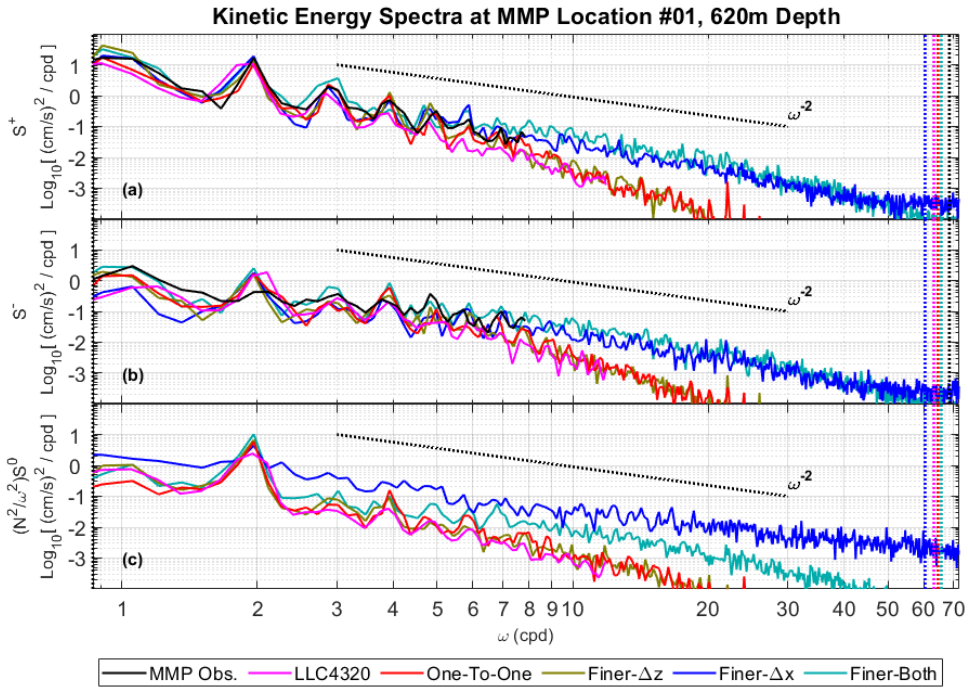

Figure 6. The total (CW plus CCW) horizontal kinetic energy spectra at 620m depth at the southern-most MMP location, including (a) the CCW kinetic energy spectra, (b) the CW kinetic energy spectra, and (c) the vertical kinetic energy spectra. The dotted curves in (a)-(c) represent the spectral slope theorized by the GM76 model. The root-mean-squares of N from each data source are plotted as vertical dotted lines colored as given in the legend and marked as N on the x-axis. These spectra are not WKBJ-scaled.

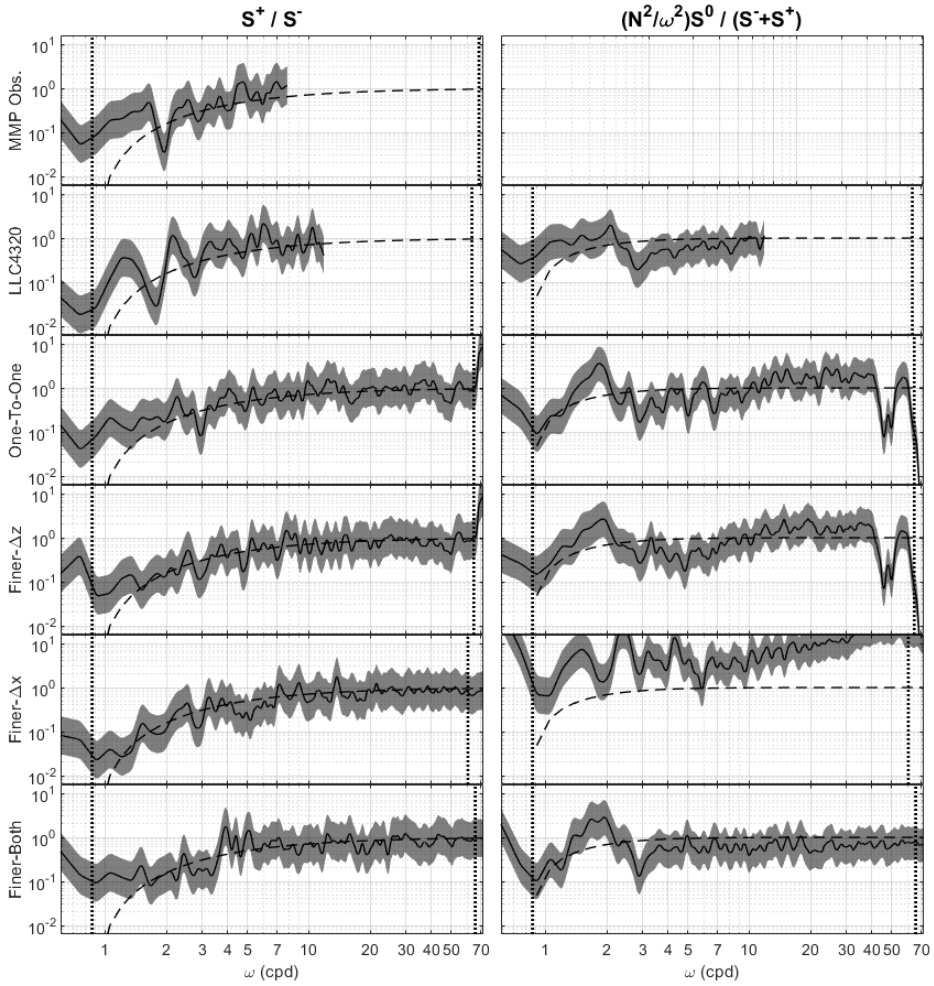

Figure 7. Consistency relations at 620m depth at the southern-most MMP location, including (left column) the ratio of CCW to CW kinetic energy spectra, and (right column) the ratio of the vertical kinetic energy spectra to the total horizontal kinetic energy spectra. Shading denotes the 90% confidence interval (5% to 95% confidence bounds).

The two consistency relations in Figure 7 are followed closely by the observations and most of the simulations except near the forcing peaks and their harmonics, but there are some notable deviations from theory. In the left column of Figure 7, which plot the ratios of the CCW to CW horizontal kinetic energy spectra, all data sources are statistically indistinguishable from theory except at frequencies approaching the Coriolis frequencies. We speculate that this may be due to the presence of other submesoscale motions such as eddies which begin to manifest at these lower frequencies, but further work is needed to verify this speculation. In addition, the observations and LLC4320 also deviate from theory at about 1 and 2 cpd due to tidal forcing, but these deviations do not show up in the regional simulations. This deviation could be due to the regional simulations beginning on the first of March rather than the beginning of the year as in LLC4320, highlighting the importance of model spin-up in the regional domain even in the presence of remote forcings.

In the right column of Figure 7, which plot the ratio of the vertical to horizontal kinetic energy spectra, the One-To-One and Finer-Δz simulations deviate significantly from theory after about 40 cpd, and the Finer-Δx simulation exhibits a ratio statistically greater than 1 at nearly all frequencies, and increases as frequency increases starting at about 10 cpd. In both plots, all data sources also exhibit a discrepancy near 2 cpd, likely due to the same reasons as discussed for the previous consistency relation. This discrepancy is consistent with results from other works (e.g. Müller et al., 1978). Note that in the Finer-Δx simulation, the consistency relation fails to hold at nearly all frequencies, once again highlighting the importance of matching the horizontal and vertical grid spacings as previously discussed. Altogether, these two consistency relations provide statistical confidence that the model does indeed simulate IWs, and that these IWs are better simulated when both horizontal and vertical grid spacings are decreased.

4.4 Vertical Wavenumber Power Spectra

The vertical wavenumber spectra computed by integrating the rotary spectra in Figure 4 across all frequencies at the southern-most MMP location are shown in Figure 8. For convenience, the CW and CCW spectra are summed together so as to reduce the number of curves on the plot. Obs.-Coarse and Obs.-Fine are the observations processed as defined in Section 3.1, and then analyzed in the same manner as the model outputs. The difference in the three observation-based spectra at low wavenumbers stems solely

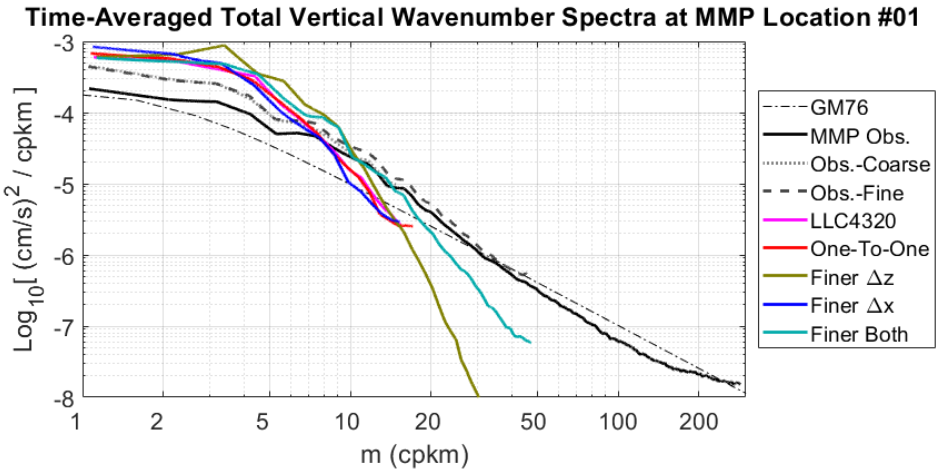

Figure 8. The record-length-averaged total (CCW+CW) vertical wavenumber spectra of horizontal velocity at the southern-most MMP location. Observations averaged within the 90-layer and 270-layer model layer configurations are labeled with dotted and dashed curves respectively.

from the WKBJ-scaling and stretching; when WKBJ is not applied, the three curves lay on top of each other (not shown). The vertical wavenumber spectrum from GM76 is included as well, and was generated using The Garrett and Munk internal wave spectra MATLAB toolbox (`http://jklymak.github.io/GarrettMunkMatlab/`).

The MMP vertical wavenumber spectra have more variance than GM76 at wavenumbers below about 30 cpkm and less variance than GM76 as higher wavenumbers. This decrease continues until the spectrum levels out beginning at about 100 cpkm. The roll-off at high m is consistent with the presence of a noise floor as found in previous work (Alford, 2010), albeit in WKBJ-stretched coordinates. There is also a roll-off at low m, but the presence of a spectral peak near 4 cpkm makes it difficult to estimate the limit at which this roll-off occurs. The theoretical value of m at which this low-m roll-off occurs in GM76 is given by (Polzin et al., 1995) as $(3\pi/Z)(N/N_0)$, where Z is the bathymetry at this location (1300km) and $N/N_0 \approx 1$, yielding a value of about 7×10^{-3} rad/m or about 1 cpkm.

In comparison to the spectra from the MMP observations, the spectra from the simulations contain more variance at low m, and less variance at high m. This pattern is strongest for the simulations with finer vertical grid spacing, and there is little improvement between the simulations with low and high horizontal grid spacing, although the

Finer-Both simulation does slightly better. This result is in agreement with the discussions at the end of Section 4.1. The simulated spectra also have their low-m roll-off beginning near 5 cpkm, and possess less distinctive spectral peaks than the observed spectrum.

In terms of agreement with observations, the Finer-Both simulation displays the greatest degree of agreement between the MMP observations and GM76 predictions, maintaining a m^{-2} slope out to about 15 cpkm, and lying closer to observations at the highest resolved vertical wavenumbers than any of the other simulations.

5 Conclusions

The primary conclusion of this work is that decreasing the model grid spacing in regional models, up to levels that are not feasible in today's global models, and using a boundary forcing which carries in remotely generated IWs, does indeed lead to a greater "filling out" of the IW spectrum and thus bringing models closer to observations and empirical models such as GM76. Along with the inclusion of remotely generated IWs, decreasing only the horizontal grid spacing significantly fills out the frequency and vertical wavenumber spectra, while decreasing only the vertical grid spacing resulted in little to no change in these spectra. Decreasing both grid spacings provides the best outcome, filling out the frequency spectrum out to the frequency of the model output (72 cpd).

The vertical wavenumber spectrum becomes arguably more deficient as the vertical grid spacing decreases without a corresponding decrease in horizontal grid spacing, with more variance observed at low wavenumbers, less variance at higher wavenumbers, and a steeper slope in between, relative to the observations. Decreasing both horizontal and vertical grid spacings does provide the best improvement in the spectra at all vertical wavenumbers, but the improvement is less substantial than the improvement seen in the frequency spectra. As hinted at by Stewart et al. (2017), the less dramatic improvement in the vertical wavenumber spectra may be due to a "mismatching" of the horizontal and vertical grid spacings, but this has not been verified.

Additionally, consistency relations for IWsderived from linear internal wave theory are applied to provide statistical confidence that the improvement seen in the IW spectrum with remote IW forcing at the boundaries and decreased grid spacing is indeed

due to IWs being generated at higher frequencies and vertical wavenumbers. However, a more in-depth investigation using, for example, theoretical frameworks for the formation of a power-law spectrum in a fluid, may provide even stronger evidence.

Models of IWs may help us to better understand the spatial geography of mixing in the ocean, and are playing an increasingly important role in planning for satellite missions (e.g., Wang et al., 2018). Improving the representation of IWs in models will benefit these research endeavors, and the results discussed here represent another step in this continual progression of improvement. In future work we plan to apply the same fine-scale parameterization techniques used to extrapolate dissipation rates from observations to IW models (e.g. Polzin et al., 1995), at least in modest-sized regions.

Acronyms

IW Internal (gravity) wave

MITgcm Massachusettes Institute of Technology global circulation model

ECMWF European Center for Medium-Range Weather Forecasts

MMP McLane Moored Profiler

WKBJ Wentzel-Kramers-Brillouin–Jeffreys

CCW Counterclockwise

CW Clockwise

Acknowledgments

ADN and BKA were supported by NASA grants NNX17AH55G and NNX16AH79G. WRP was supported by the Natural Sciences and Engineering Research Council of Canada under NSERC Discovery grant A9627. NG was supported under NSERC Discovery Grant RGPIN-2015-03684 and Canadian Space Agency grant 14SUSWOTTO. The computations described in this paper were performed on the Niagara supercomputer of the SciNet facility of the University of Toronto, which is a component of the Compute Canada HPC platform. The observations and MMP-sampled modeled data used in this study are open-access and hosted at the University of Michigan Deep Blue Data repository at `https://deepblue.lib.umich.edu/data/concern/data_sets/9s1616296`. The MMP observations from Alford et al. (2007) were funded by NSF and used with permission and provided by Gunnar Voet at Scripps. The MMP observations would not have been possi-

ble without the talent and hard work of the captain, Tom DesJardines, and crew of R/V Revelle. The authors also wish to thank Eric Kunze for insightful discussions about the importance of WKBJ stretching, and Carl Wunsch, Dirk Olbers, and Ren-Chieh Lien for suggesting that we test IGW models using consistency relations.

References

Alford, M. (2010). Sustained, full–water–column observations of internal waves and mixing near Mendocino Escarpment. *Journal of Physical Oceanography*, *40*(12), 2643-2660. doi: 10.1175/2010JPO4502.1

Alford, M., MacKinnon, J., Pinkel, R., & Klymak, J. (2017). Space-time scales of shear in the North Pacific. *Journal of Physical Oceanography*, *47*(10), 2455–2478. doi: 10.1175/JPO-D-17-0087.1

Alford, M., MacKinnon, J., Zhao, Z., Pinkel, R., Klymak, J., & Peacock, T. (2007). Internal waves across the Pacific. *Geophysical Research Letters*, *34*(24). doi: 10.1029/2007GL031566

Alford, M., & Whitmont, M. (2007). Seasonal and spatial variability of near-inertial kinetic energy from historical moored velocity records. *Journal of Physical Oceanography*, *37*(8), 2022–2037.

Arbic, B., et al. (2018). A primer on global internal tide and internal gravity wave continuum modeling in HyCOM and MITgcm. In E. Chassignet, A. Pascual, J. Tintore, & J. Verron (Eds.), *New Frontiers in Operational Oceanography*. GODAE OceanView.

Arbic, B., Wallcraft, A., & Metzger, E. (2010). Concurrent simulation of the eddying general circulation and tides in a global ocean model. *Ocean Modelling*, *32*(3), 175 - 187. (The magic of modelling: A special volume commemorating the contributions of Peter D. Killworth Part 2) doi: https://doi.org/10.1016/j.ocemod.2010.01.007

Bretthorst, G. (2003). Frequency estimation and generalized Lomb-Scargle periodograms. In E. Feigelson & G. Babu (Eds.), *Statistical challenges in astronomy* (p. 309-329).

Chassignet, E., Hurlburt, H., Metzger, E., Smedstad, O., Cummings, J., Halliwell, G., ... others (2009). US GODAE: Global ocean prediction with the HYbrid Coordinate Ocean Model (HYCOM). *Oceanography*, *22*(2), 64–75.

Fofonoff, N. (1969). Spectral characteristics of internal waves in ocean. *Deep-Sea Research*, 59.

Fu, L.-L., Alsdorf, D., Morrow, R., Rodrigues, E., & Mognard, N. (2012). SWOT: The Surface Water and Ocean Topography Mission - Wide-swath altimetric measurement of water elevation on Earth. *JPL Publication*, *12*(5). Retrieved from `http://swot.jpl.nasa.gov/files/SWOT_MSD_final-3-26-12.pdf`

Garrett, C., & Munk, W. (1972). Space-time scales of internal waves. *Geophysical Fluid Dynamics*, *3*(1), 225-264. doi: 10.1080/03091927208236082

Garrett, C., & Munk, W. (1975). Space–time scales of internal waves: A progress report. *Journal of Geophysical Research*, *80*(3), 291-297. doi: 10.1029/JC080i003p00291

Garrett, C., & Munk, W. (1979). Internal waves in the ocean. *Annual Review of Fluid Mechanics*, *11*(1), 339-369. doi: 10.1146/annurev.fl.11.010179.002011

Large, W., & Yeager, S. (2004). *Diurnal to decadal global forcing for ocean and sea-ice models: The data sets and flux climatologies* (NCAR Technical Note NCAR/TN-460+STR). doi: 10.5065/D6KK98Q6

Leaman, K., & Sanford, T. (1975). Vertical energy propagation of inertial waves: A vector spectral analysis of velocity profiles. *Journal of Geophysical Research*, *80*(15), 1975–1978. doi: 10.1029/JC080i015p01975

Levine, M. (2002). A modification of the Garrett-Munk internal wave spectrum. *Journal of Physical Oceanography*, *32*, 3166-3181. doi: 10.1175/1520-0485(2002)032⟨3166:AMOTGM⟩2.0.CO;2

Lien, R.-C., & Müller, P. (1992). Consistency relations for gravity and vortical modes in the ocean. *Deep Sea Research Part A. Oceanographic Research Papers*, *39*(9), 1595 – 1612. doi: https://doi.org/10.1016/0198-0149(92)90050-4

Lomb, N. (1976). Least-squares frequency analysis of unequally spaced data. *Astrophysics and space science*, *39*(2), 447–462.

Losch, M., Menemenlis, D., Campin, J.-M., Heimbach, P., & Hill, C. (2010). On the formulation of sea-ice models. Part 1: Effects of different solver implementations and parameterizations. *Ocean Modelling*, *33*(1-2), 129–144.

Luecke, C., Arbic, B., Bassette, S., Richman, J., Shriver, J., Alford, M., ... Wallcraft, A. (2017). The global mesoscale eddy available potential energy field in models and observations. *Journal of Geophysical Research: Oceans*, *122*(11),

9126-9143. doi: 10.1002/2017JC013136

MacKinnon, J., St. Laurent, L., Garabato, N., & Alberto, C. (2013). Diapycnal mixing processes in the ocean interior. In G. Siedler, S. Griffies, J. Gould, & J. Church (Eds.), *Ocean circulation and climate: A 21st century perspective* (Vol. 103, p. 159-183). Academic Press. doi: 10.1016/B978-0-12-391851-2.00007-6

Marshall, J., Hill, C., Perelman, L., & Adcroft, A. (1997). Hydrostatic, quasi-hydrostatic, and nonhydrostatic ocean modeling. *Journal of Geophysical Research: Oceans*, *102*(C3), 5733-5752. doi: 10.1029/96JC02776

Mazloff, M. R., Cornuelle, B., Gille, S. T., & Wang, J. (2020). The importance of remote forcing for regional modeling of internal waves. *Journal of Geophysical Research: Oceans*, *125*(2), e2019JC015623. doi: 10.1029/2019JC015623

McDougall, T., & Barker, P. (2011). Getting started with TEOS-10 and the Gibbs Seawater (GSW) oceanographic toolbox. *SCOR/IAPSO WG*, *127*, 1–28.

Morrison III, A., Toole, R., J .and Lukas, Worrilow, S., & Doherty, K. (2001). Results from the first successful field deployment of the Mclane Moored Profiler. In *MTS/IEEE Oceans 2001. An Ocean Odyssey. Conference Proceedings (IEEE Cat. No.01CH37295)* (Vol. 2, p. 949 - 955). doi: 10.1109/OCEANS.2001.968243

Müller, M., Arbic, B., Richman, J., Shriver, J., Kunze, E., Scott, R., ... Zamudio, L. (2015). Toward an internal gravity wave spectrum in global ocean models. *Geophysical Research Letters*, *42*(9), 3474-3481. doi: 10.1002/2015GL063365

Müller, P., Olbers, D., & Willebrand, J. (1978). The IWEX spectrum. *Journal of Geophysical Research*, *83*, 479–500. doi: 10.1029/JC083iC01p00479

Müller, P., & Siedler, G. (1976). Consistency relations for internal waves. In *Deep sea research and oceanographic abstracts* (Vol. 23, pp. 613–628).

Munk, W., & Wunsch, C. (1998). Abyssal recipes II: Energetics of tidal and wind mixing. *Deep Sea Research Part I: Oceanographic Research Papers*, *45*(12), 1977 - 2010. Retrieved from `http://www.sciencedirect.com/science/article/pii/S0967063798000703` doi: https://doi.org/10.1016/S0967-0637(98)00070-3

Nansen, F. (1897). *Farthest North: The epic adventure of a visionary explorer*. Skyhorse Publishing.

Polzin, K., Toole, J., & Schmitt, R. (1995). Finescale parameterizations of turbulent dissipation. *Journal of Physical Oceanography*, *25*(3), 306-328. doi: 10.1175/1520-0485(1995)025⟨0306:FPOTD⟩2.0.CO;2

Ponce, M., van Zon, R., Northrup, S., Gruner, D., Chen, J., Ertinaz, F., ... others (2019). Deploying a top-100 supercomputer for large parallel workloads: the Niagara Supercomputer. In *Proceedings of the practice and experience in advanced research computing on rise of the machines (learning)* (p. 34).

Ponte, R., Chaudhuri, A., & Vinogradov, S. (2015). Long-period tides in an atmospherically driven, stratified ocean. *Journal of Physical Oceanography*, *45*(7), 1917–1928.

Qiu, B., Chen, S., Klein, P., Wang, J., Torres, H., Fu, L.-L., & Menemenlis, D. (2018). Seasonality in transition scale from balanced to unbalanced motions in the World Ocean. *Journal of Physical Oceanography*, *48*(3), 591-605. doi: 10.1175/JPO-D-17-0169.1

Rocha, C., Gille, S., Chereskin, T., & Menemenlis, D. (2016). Seasonality of submesoscale dynamics in the Kuroshio Extension. *Geophysical Research Letters*, *43*(21), 11–304.

Savage, A., Arbic, B., Alford, M., Ansong, J., Farrar, J., Menemenlis, D., ... Zamudio, L. (2017). Spectral decomposition of internal gravity wave sea surface height in global models. *Journal of Geophysical Research: Oceans*, *122*(10), 7803-7821. doi: 10.1002/2017JC013009

Scargle, J. (1982). Studies in astronomical time series analysis. II-Statistical aspects of spectral analysis of unevenly spaced data. *The Astrophysical Journal*, *263*, 835–853.

Shriver, J., Arbic, B., Richman, J., Ray, R., Metzger, E., Wallcraft, A., & Timko, P. (2012). An evaluation of the barotropic and internal tides in a high-resolution global ocean circulation model. *Journal of Geophysical Research: Oceans*, *117*(C10). doi: 10.1029/2012JC008170

Stewart, K., Hogg, A., Griffies, S., Heerdegen, A., Ward, M., Spence, P., & England, M. (2017). Vertical resolution of baroclinic modes in global ocean models. *Ocean Modelling*, *113*, 50 - 65. doi: 10.1016/j.ocemod.2017.03.012

Toole, J. (2001). McLane Moored Profiler data reduction and processing procedures [Computer software manual]. Retrieved from `ftp://flotsam.whoi.edu/`

`matfiles/MP_software/How_To/readme_MMP_proc.html`

Wang, J., Fu, L.-L., Qiu, B., Menemenlis, D., Farrar, J., Chao, Y., ... Flexas, M. (2018). An observing system simulation experiment for the calibration and validation of the Surface Water Ocean Topography sea surface height measurement using in situ platforms. *Journal of Atmospheric and Oceanic Technology*, *35*(2), 281-297. doi: 10.1175/JTECH-D-17-0076.1

Yu, X., Ponte, A., Elipot, S., Menemenlis, D., Zaron, E., & Abernathey, R. (2019). Surface kinetic energy distributions in the global oceans from a high-resolution numerical model and surface drifter observations. *Geophysical Research Letters*. doi: 10.1029/2019GL083074

Zhao, Z., Alford, M., MacKinnon, J., & Pinkel, R. (2010). Long-range propagation of the semidiurnal internal tide from the Hawaiian Ridge. *Journal of Physical Oceanography*, *40*(4), 713-736. doi: 10.1175/2009JPO4207.1

Figure 1.

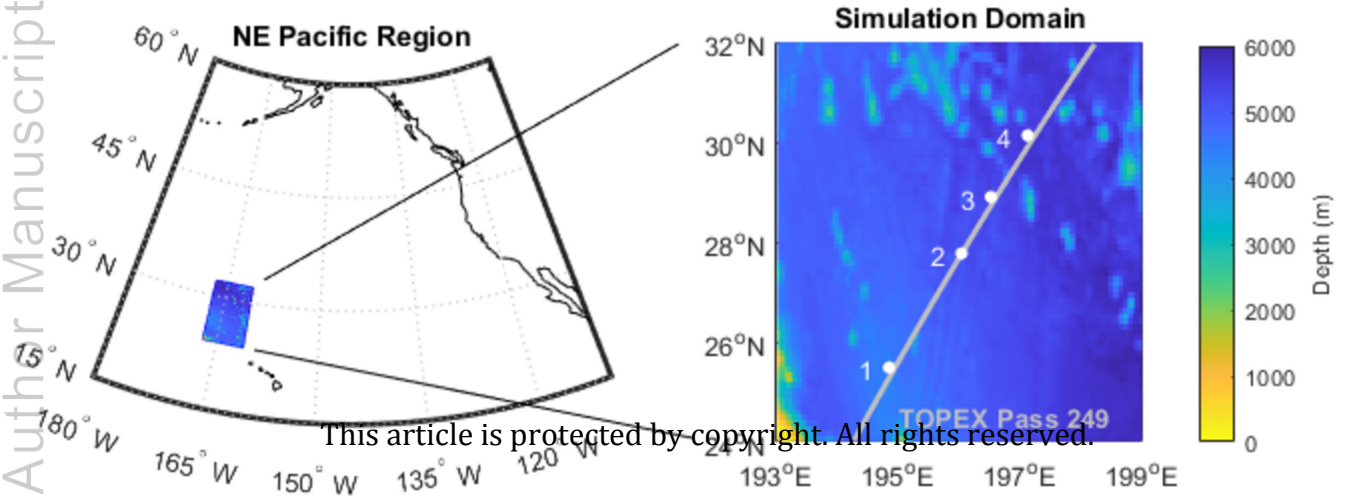

Figure 2.

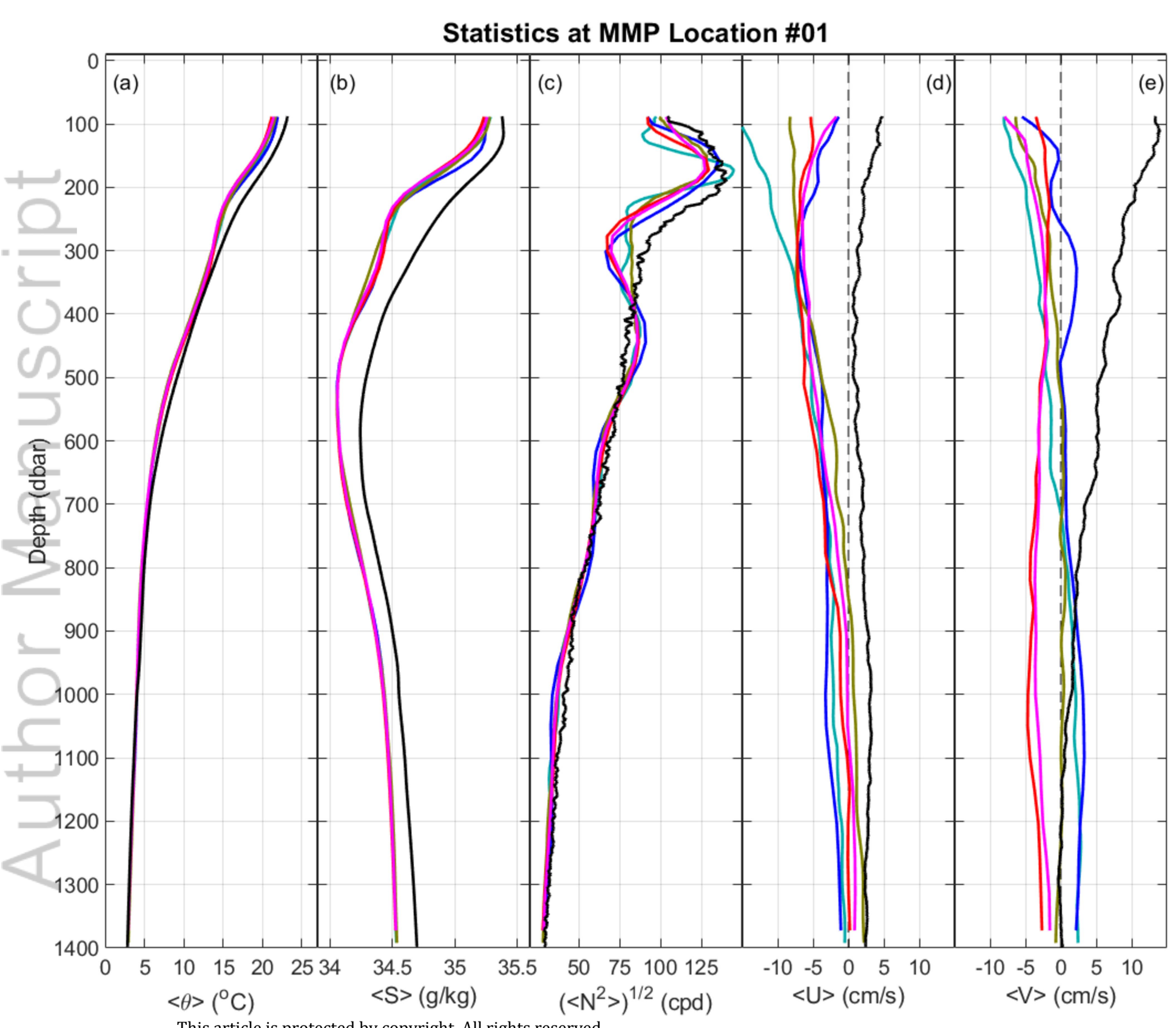

Figure 3.

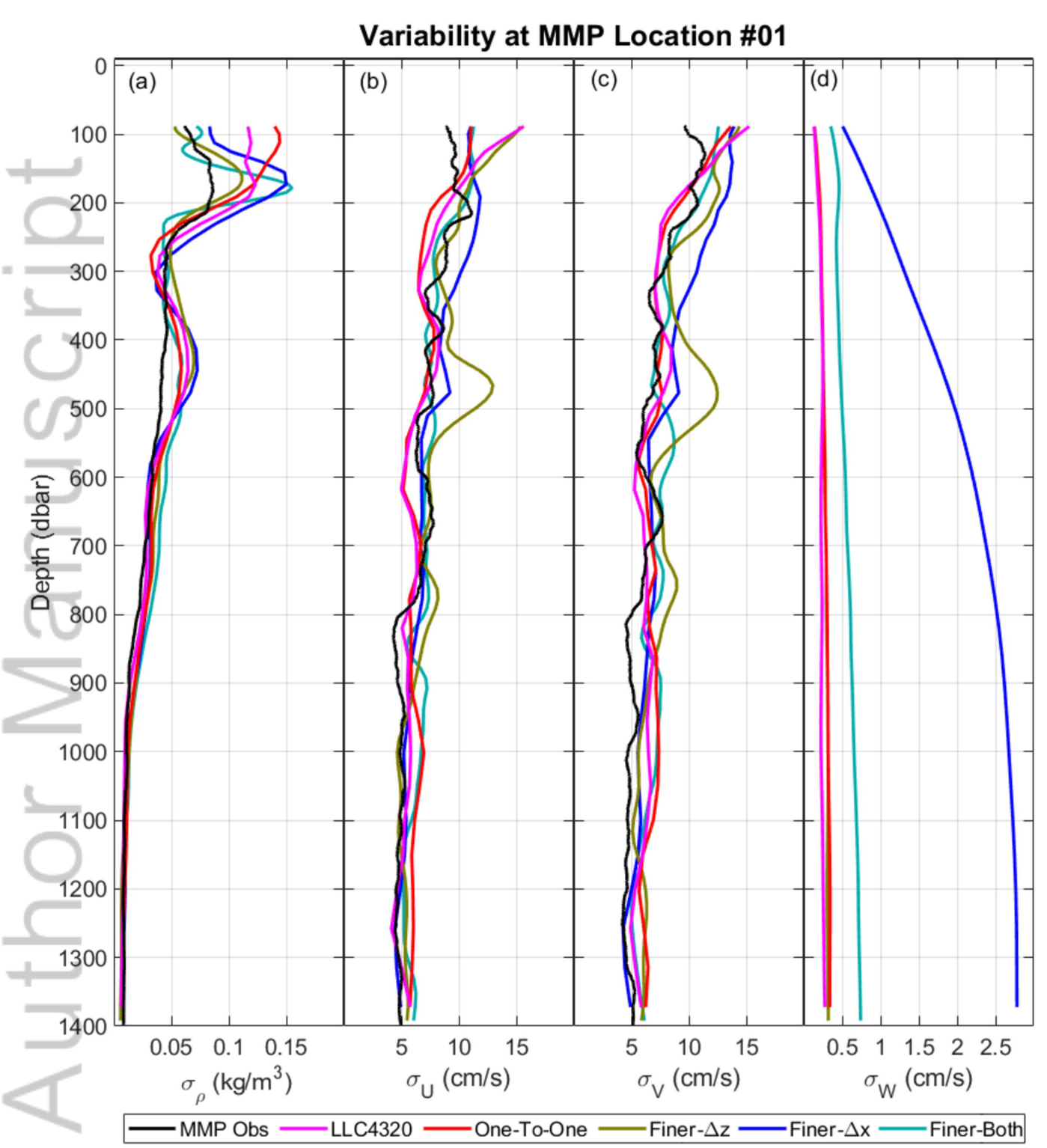

Figure 4.

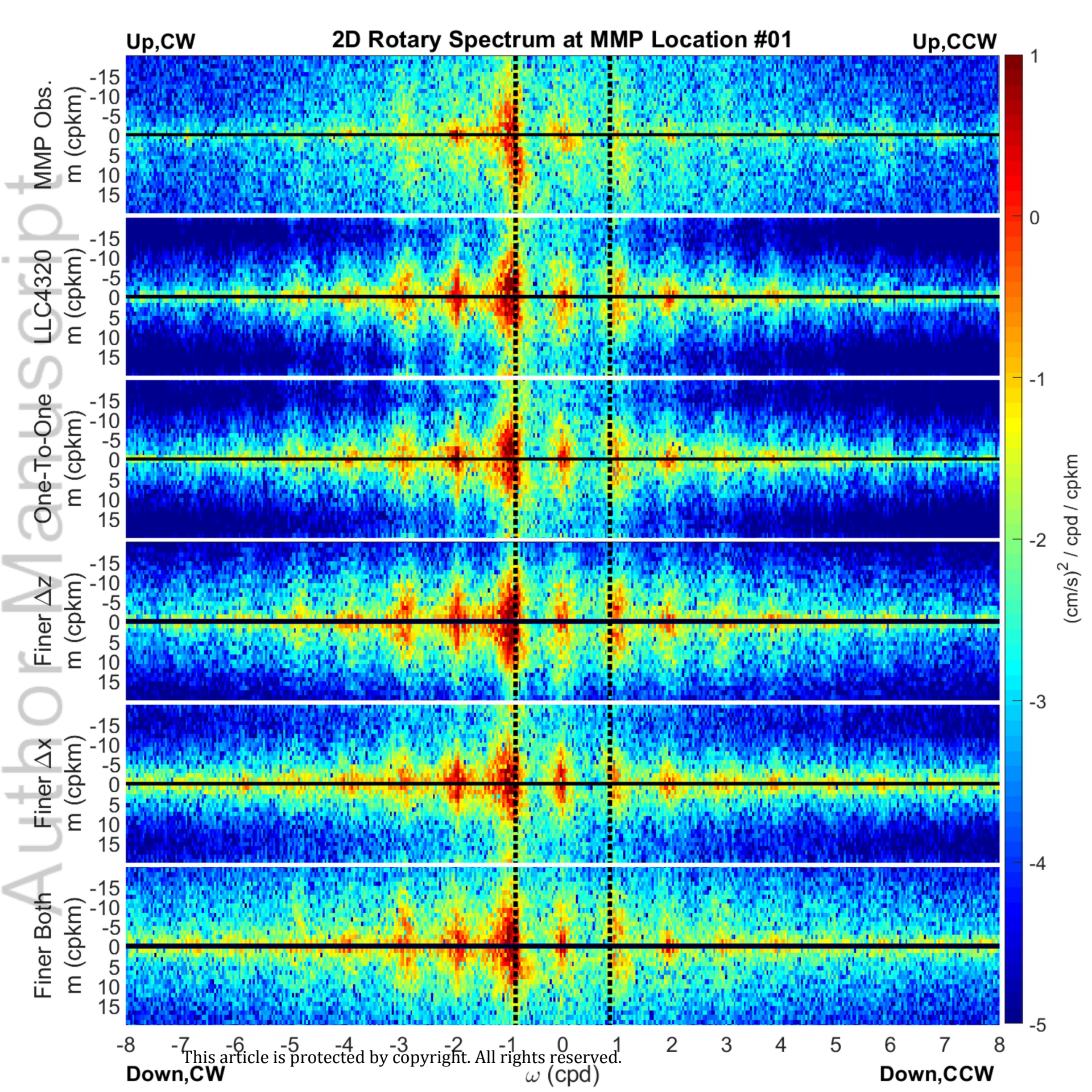

Figure 5.

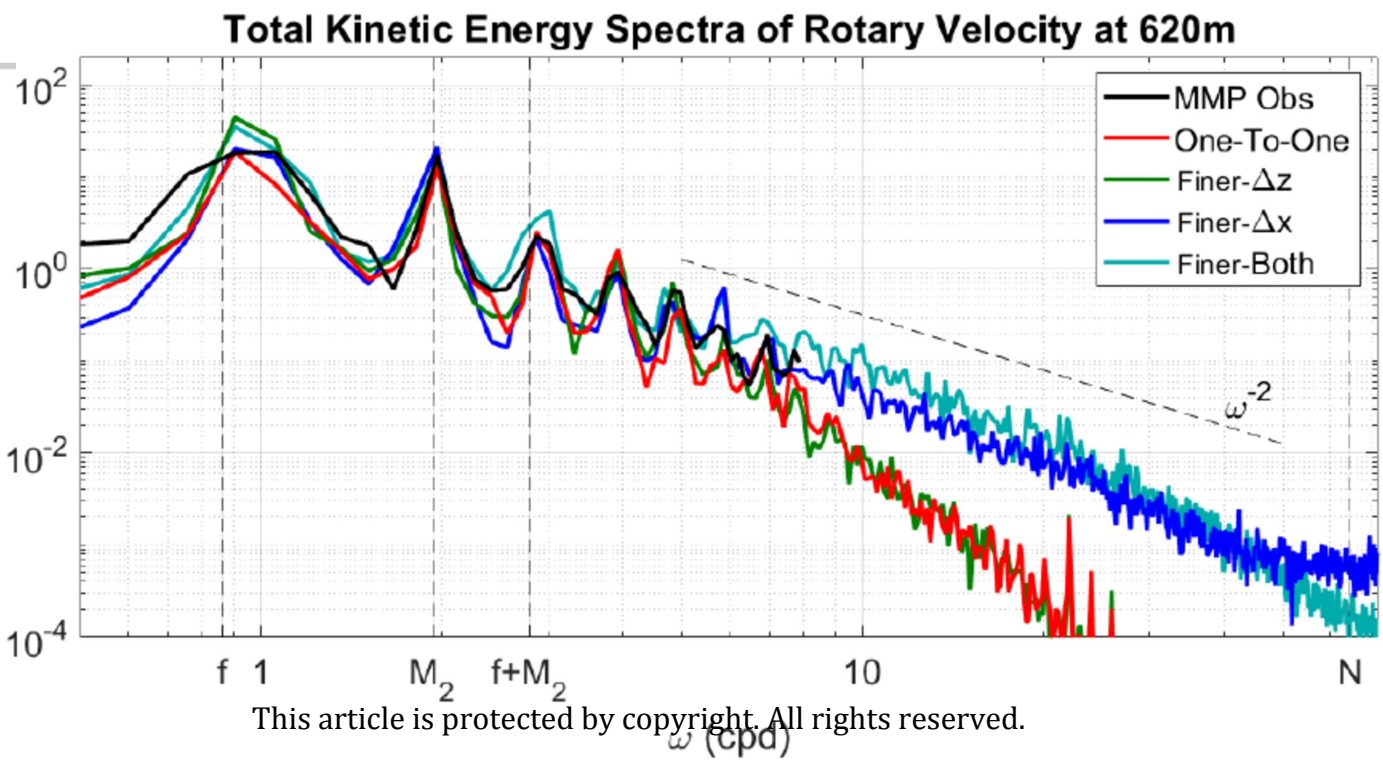

Figure 6.

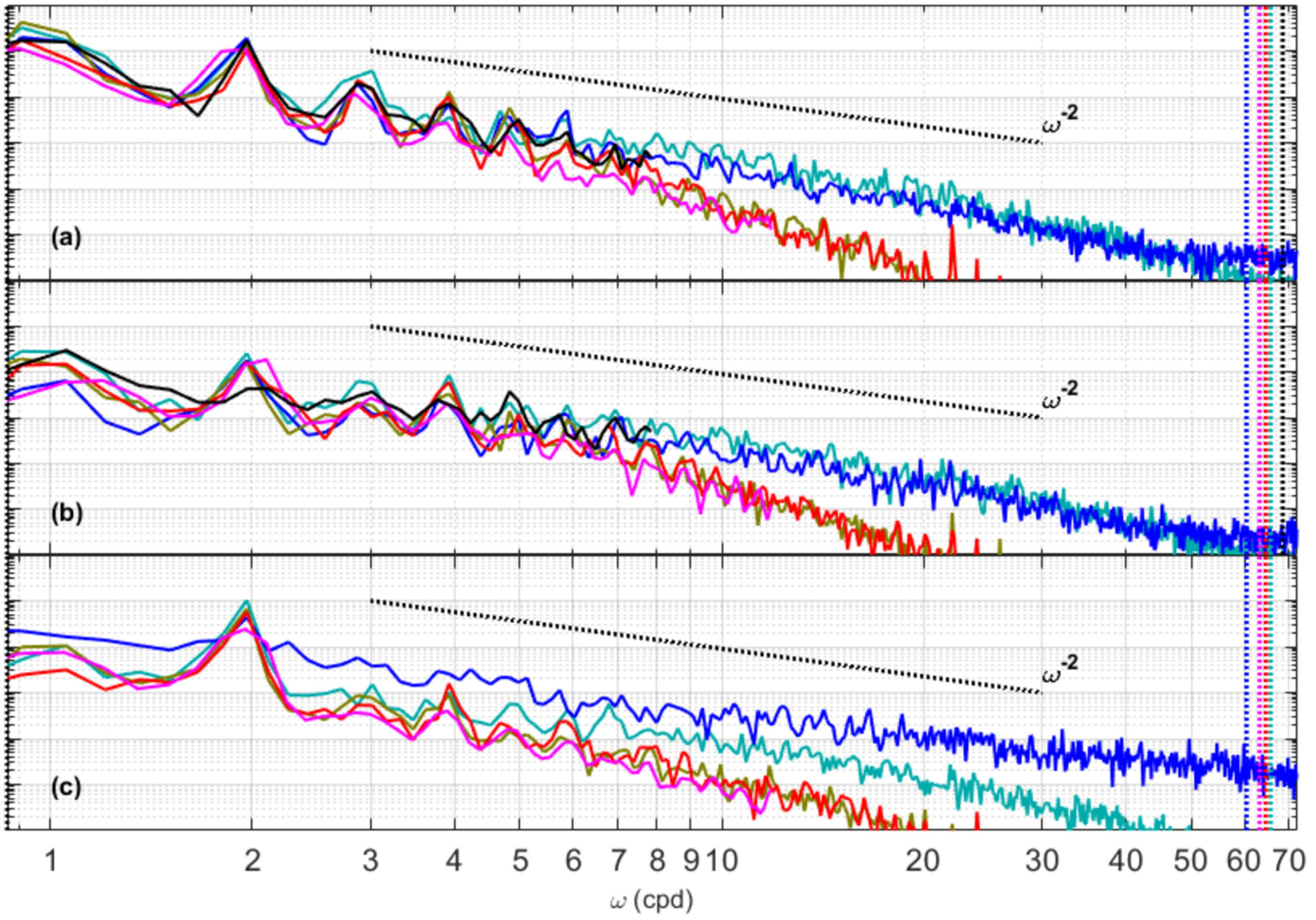

Figure 7.

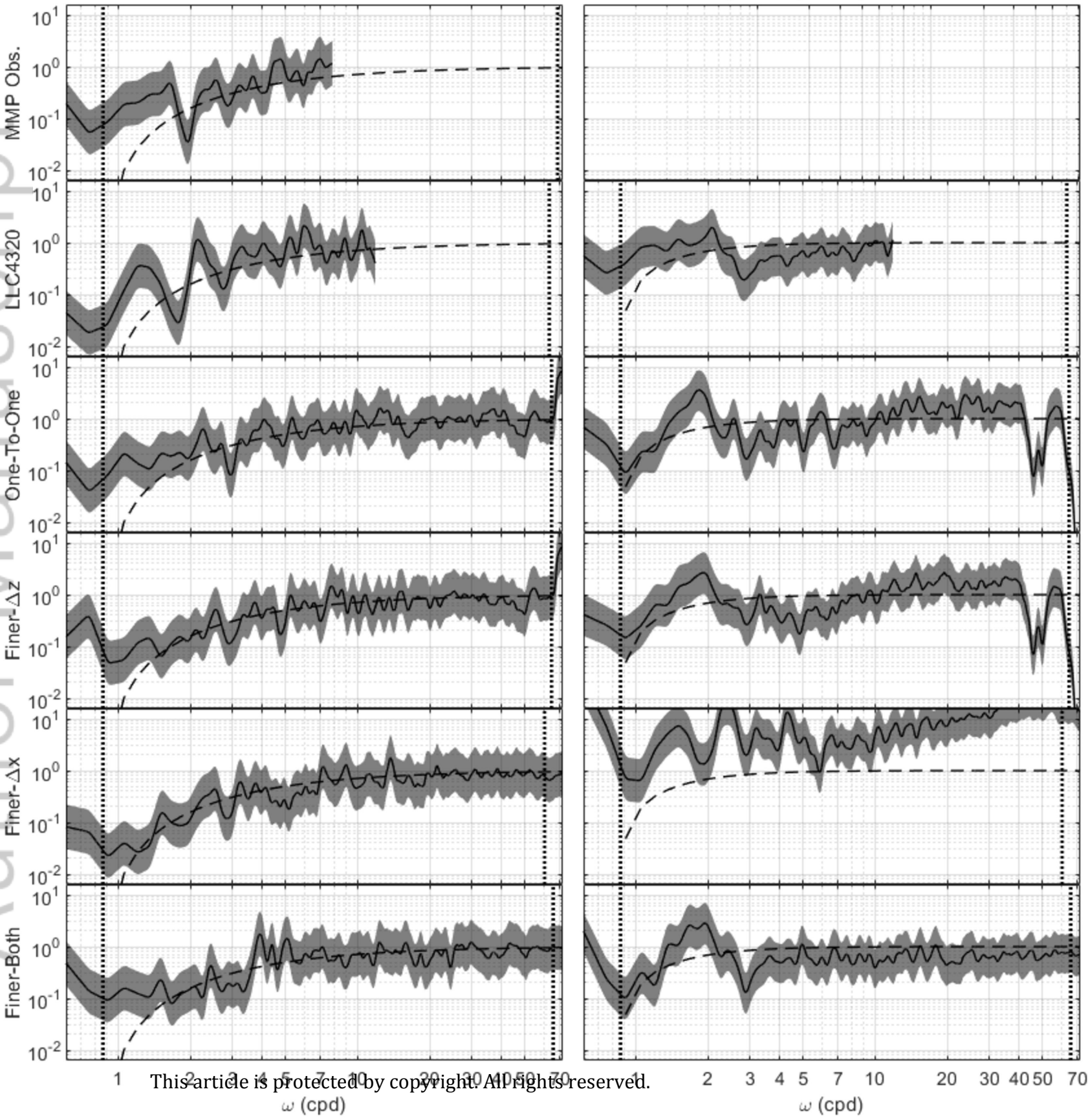

Figure 8.

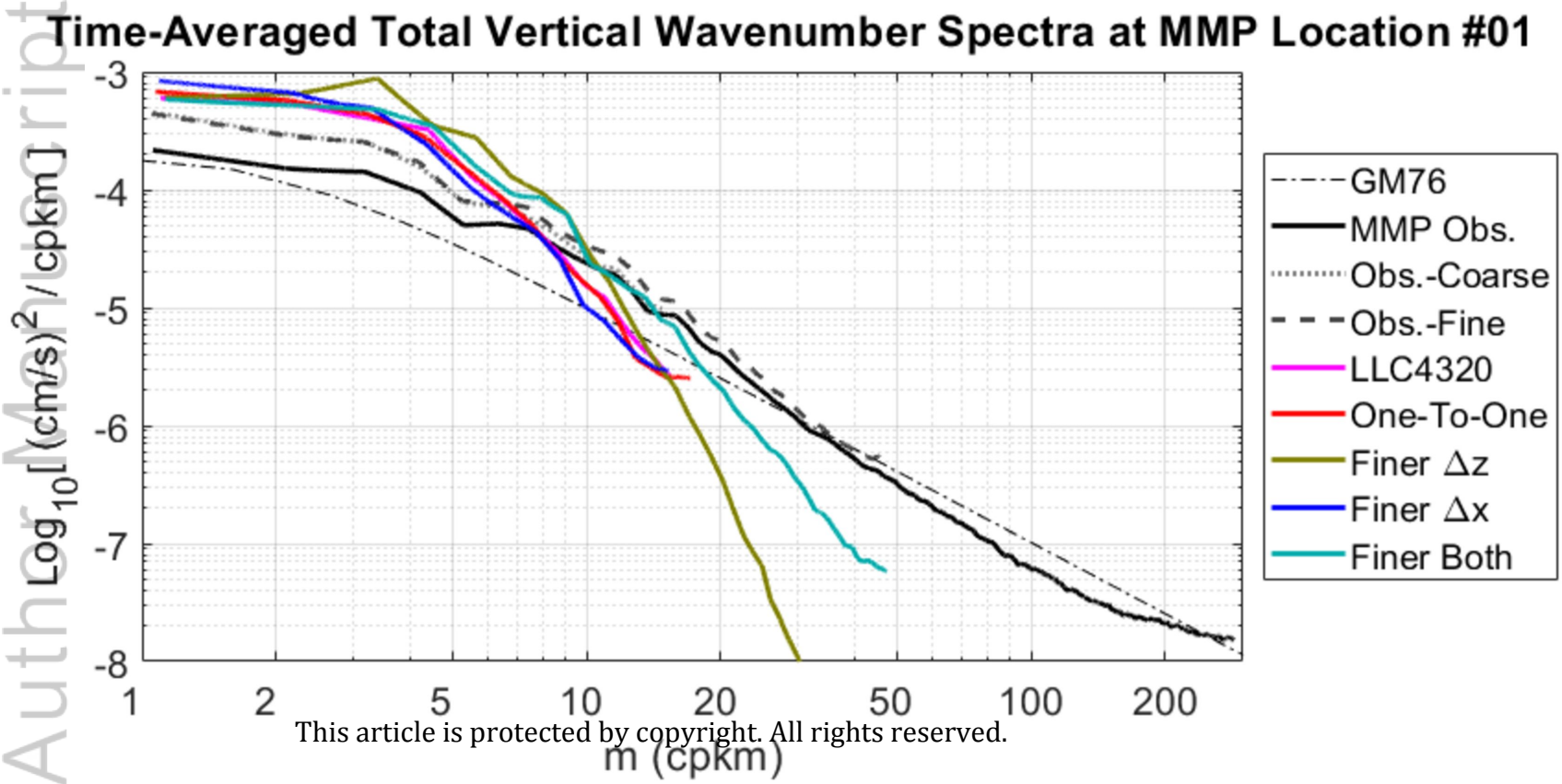

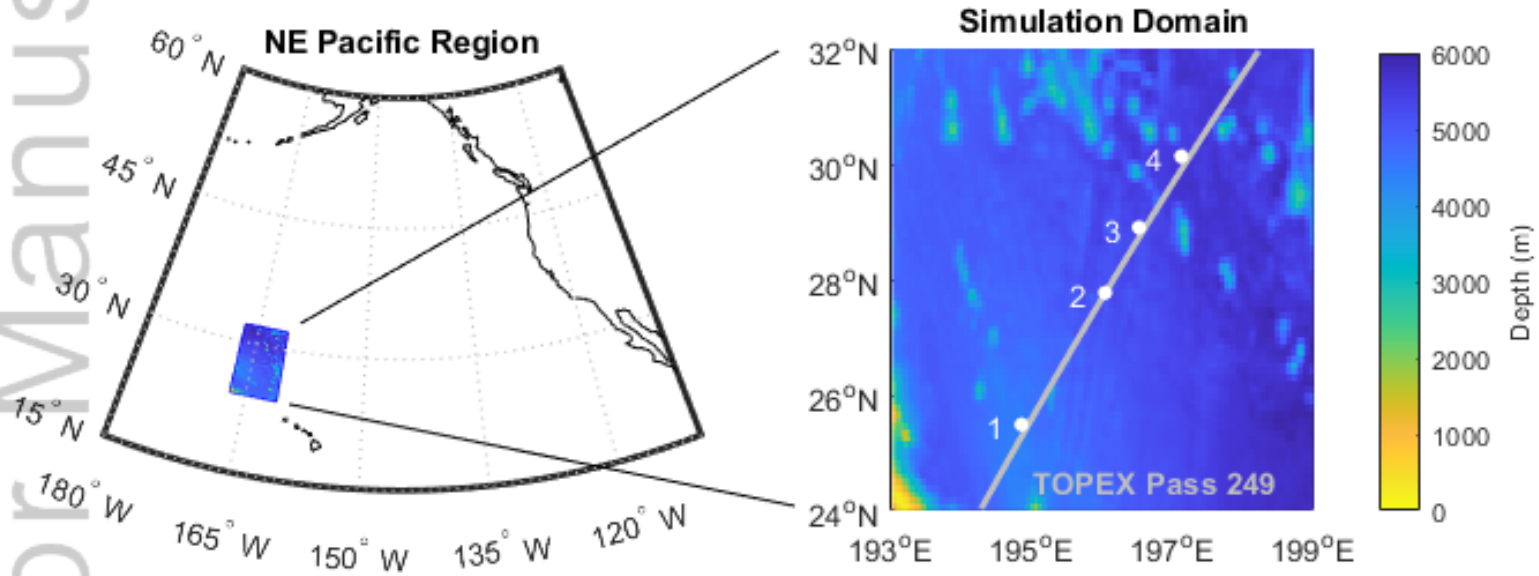

2019JC015974-f01-z-.png

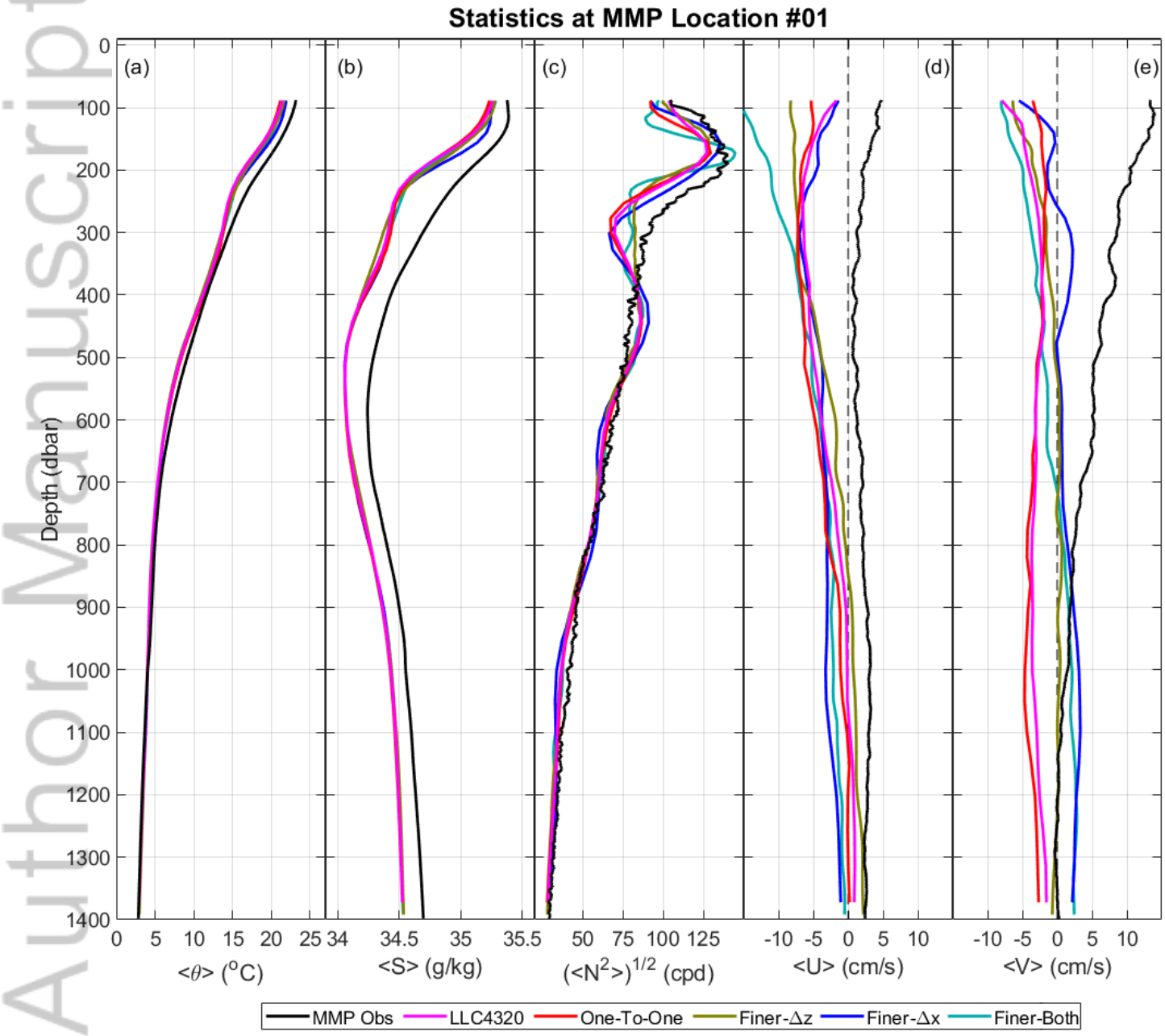

2019JC015974-f02-z-.png

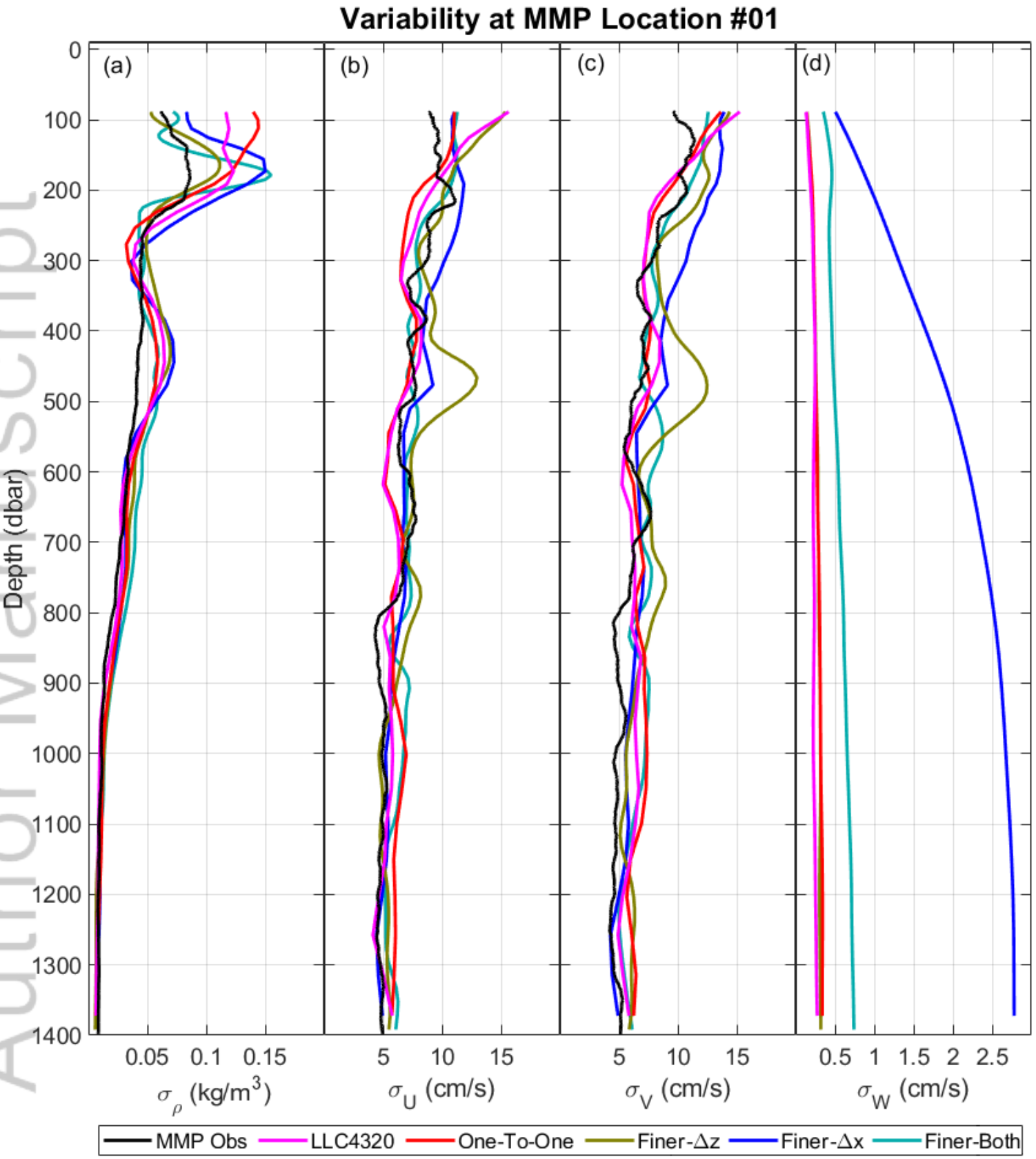

2019JC015974-f03-z-.png

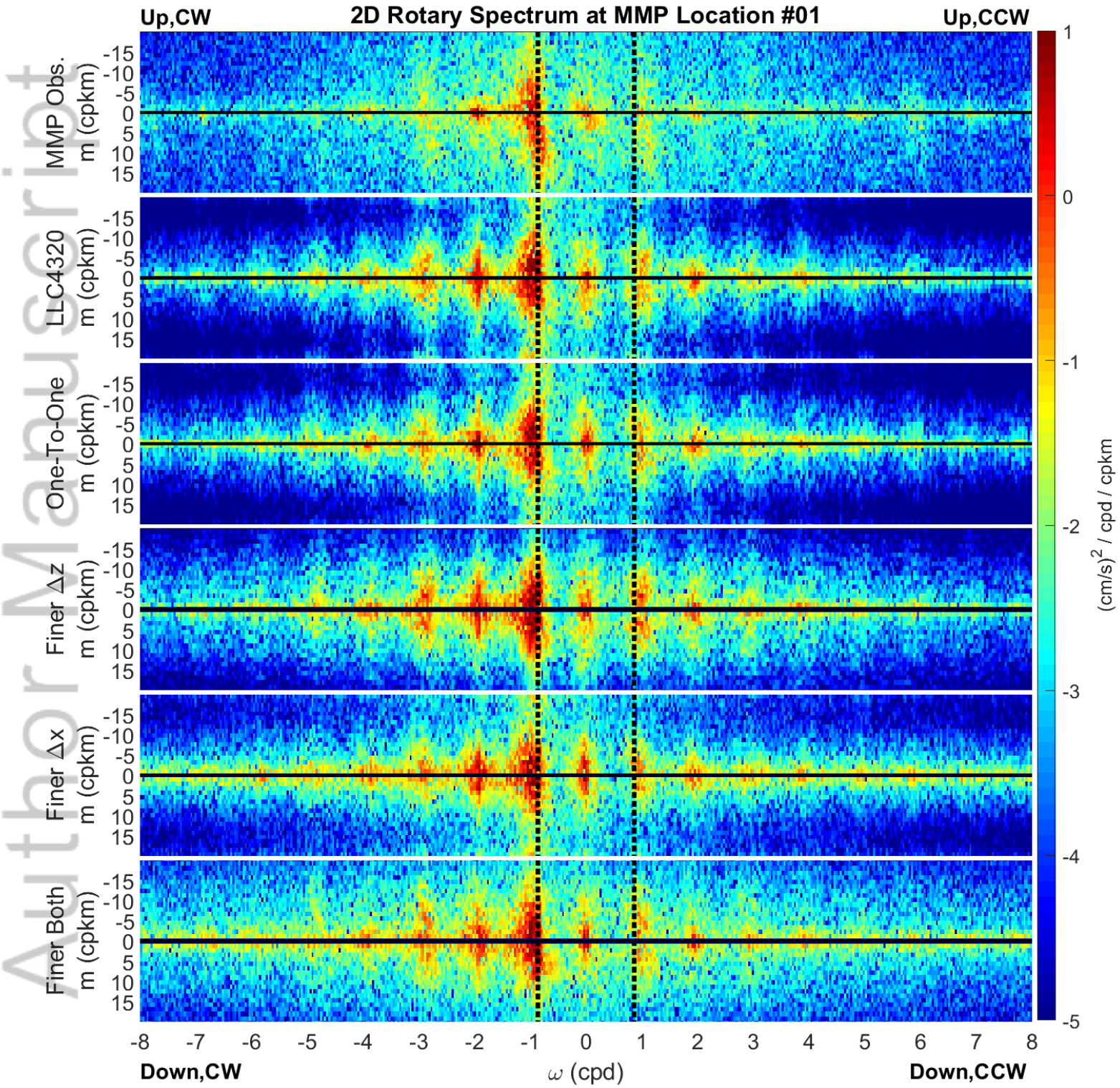

2019JC015974-f04-z-.png

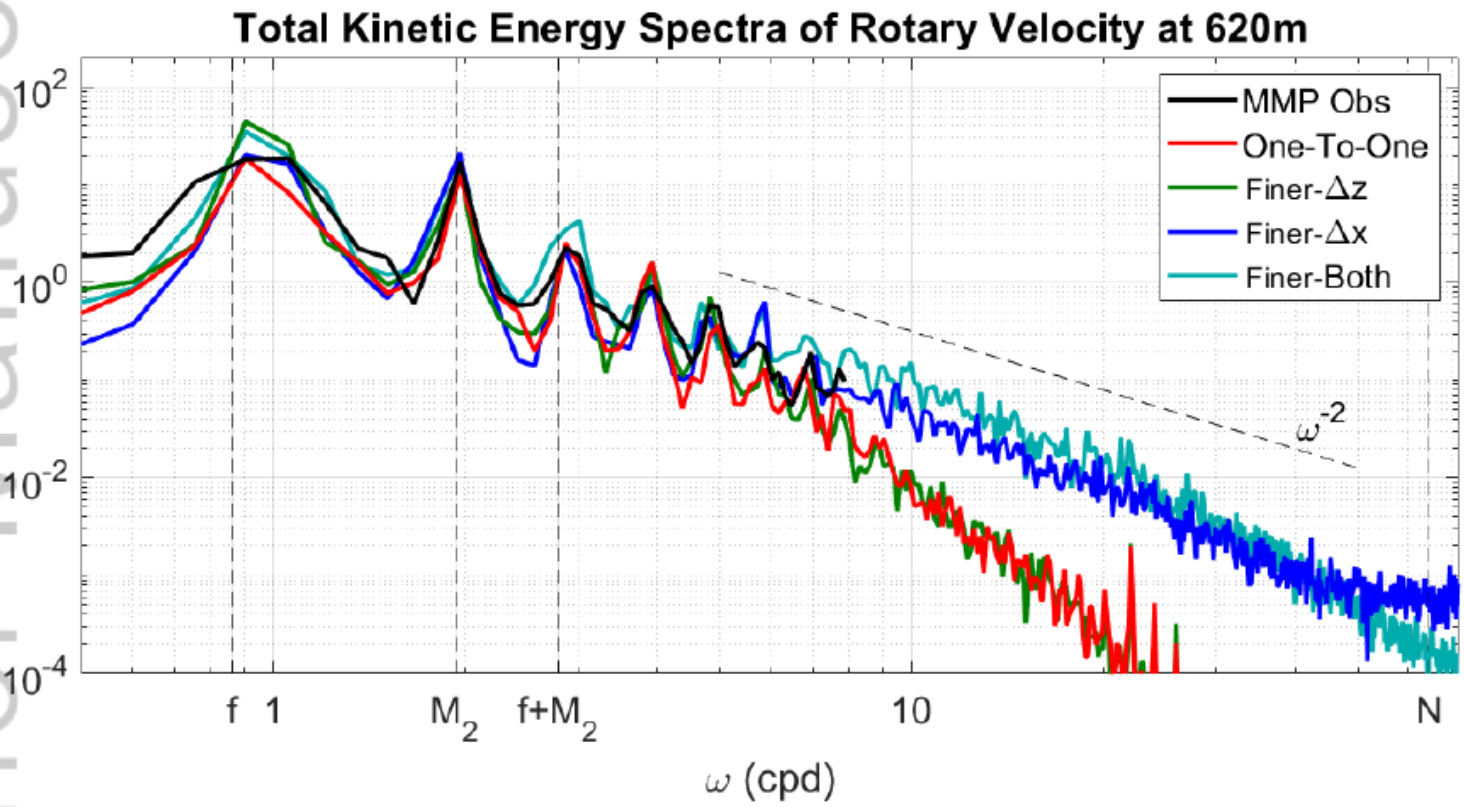

2019JC015974-f05-z-.png

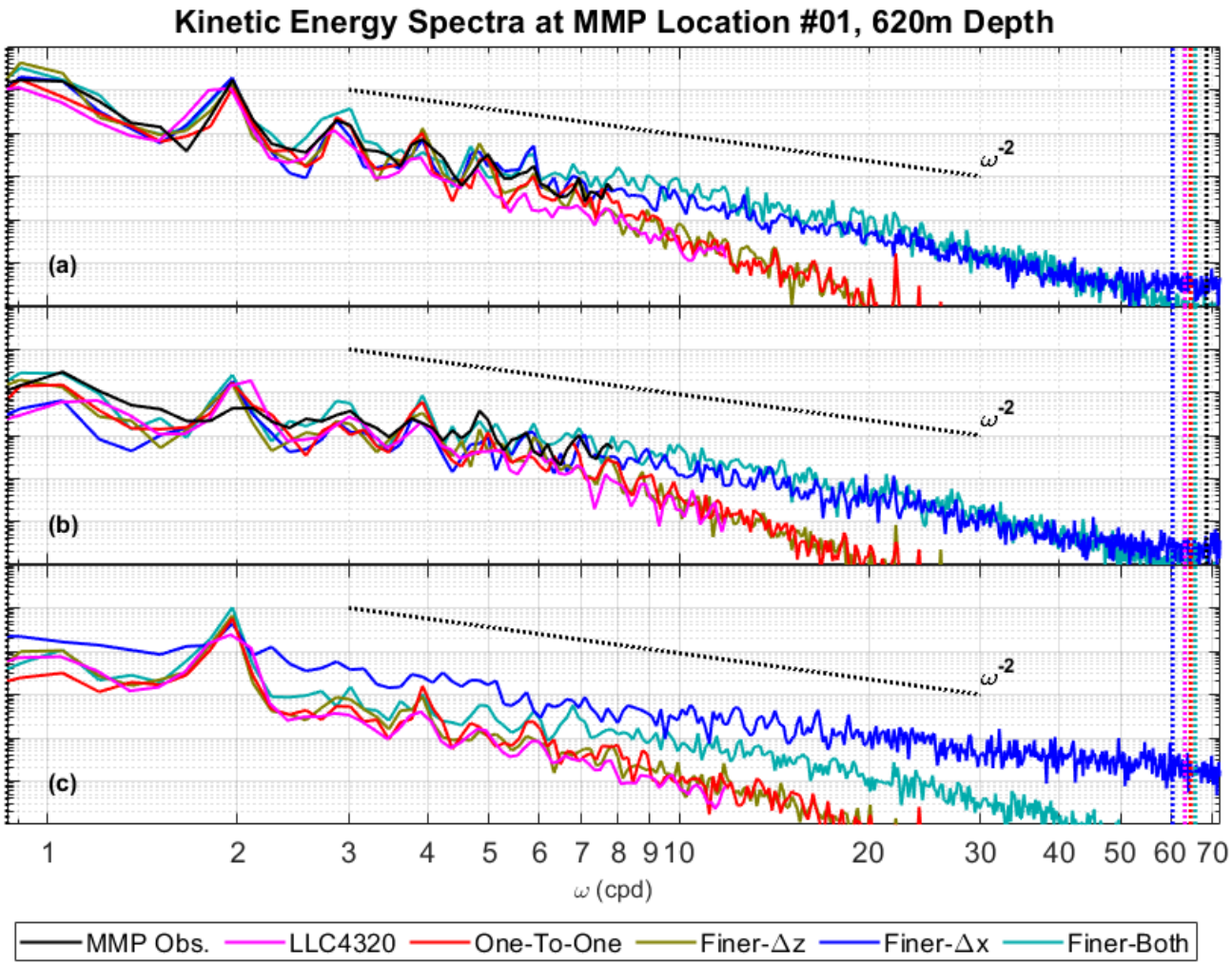

2019JC015974-f06-z-.png

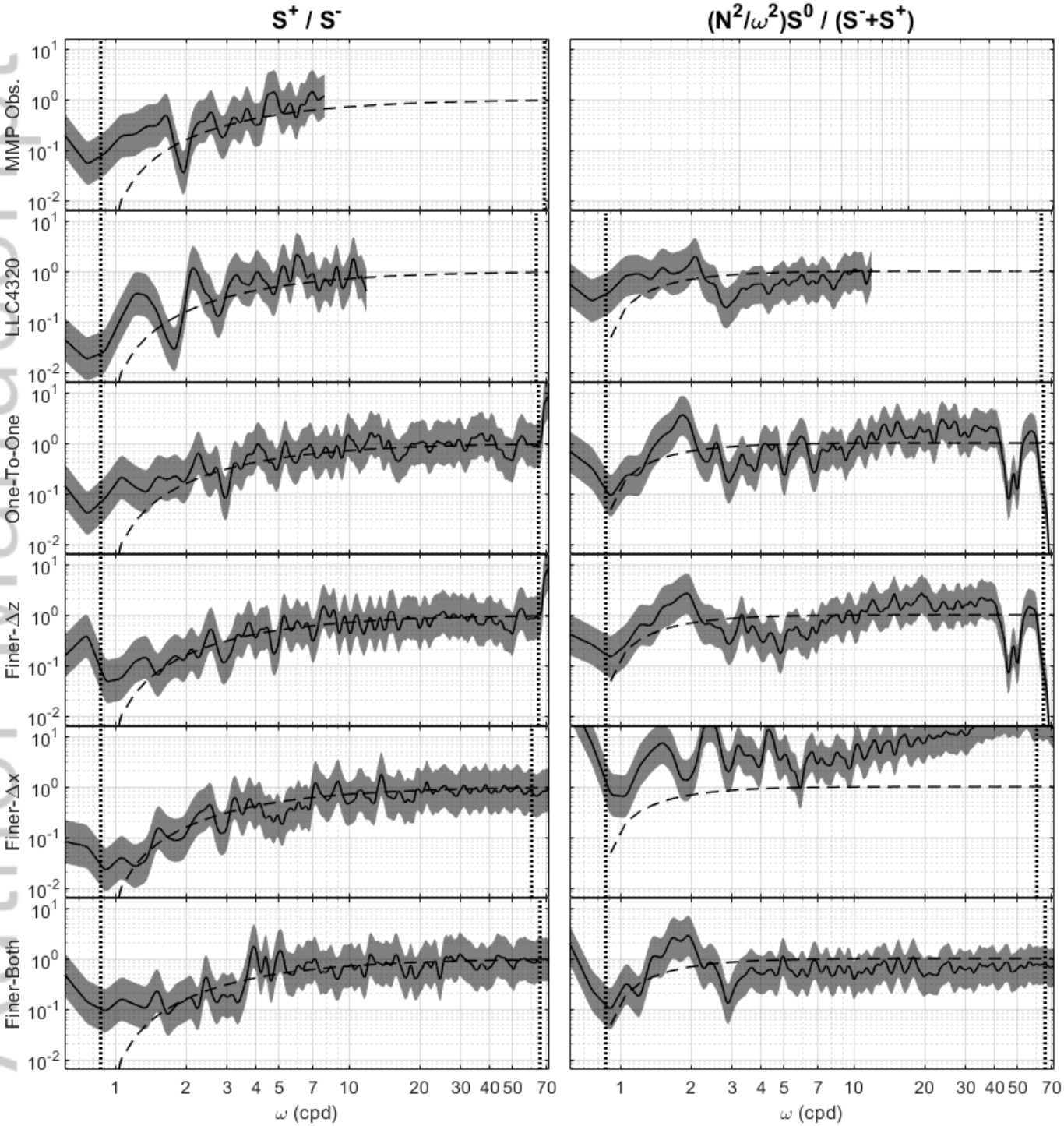

2019JC015974-f07-z-.png

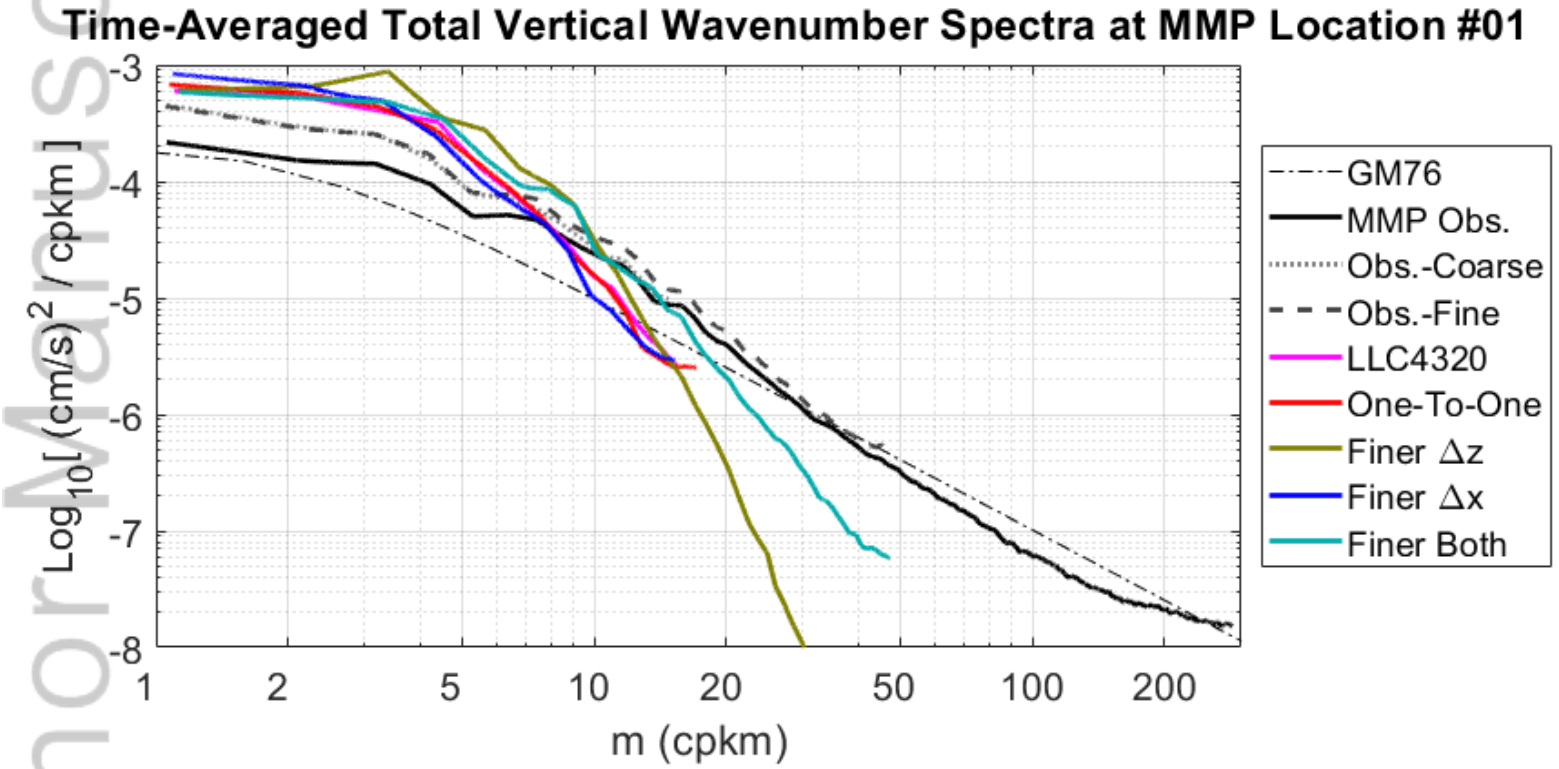

2019JC015974-f08-z-.png